Should You Split Decode? Disaggregation Across Future Models and Accelerators

Ramyad Hadidi†

arXiv:2611.08299v1 [cs.AR] 5 Nov 2026

***Abstract*—For large language model (LLM) inference, prefill/decode disaggregation (P/D) is deployed in production to isolate phases with different resource demands. Attention/feed-forward network disaggregation (AFD) splits decode again, but adds communication, placement constraints, and another provisioned pool. We ask whether role-specific placement repays this cost as models and accelerator roadmaps change. Infrastructure is committed before future models and hardware can be benchmarked. We present SILICONFORGE, a calibrated model that varies the serving decomposition and hardware assignment independently. We compare P/D and P/D+AFD across four model directions, four accelerator classes anchored to current and announced parts, and two fabrics. We co-optimize each design using the same rules for pipeline overlap and the same power budget. Our main comparisons show no robust deployment-level AFD advantage in service-level objective (SLO) goodput per kW. Most nominal estimates favor P/D. The largest AFD lead comes from fitting one more prefill replica, not from a more efficient decode pool. AFD has a nominal lead in the KV-heavy (key–value) model direction when the co-located expert pool spans several small scale-up domains. Larger domains or a fast fabric for both designs weaken that lead. We therefore find that prefill provisioning, decode memory bandwidth, links, and pool granularity decide deployments more than the split alone. A fixed hardware assignment can lose its advantage as models, fabrics, hardware assumptions, and objectives change. Re-optimizing mappings and pool sizes on the same hardware cuts early commitment's median normalized goodput loss from 36% to 9%. We recommend adjustable mappings and pool sizes to let boundary and hardware choices follow model demands.**

I. INTRODUCTION

Accelerator roadmaps for large language model (LLM) inference trade compute, memory bandwidth, capacity, interconnect, and power, while prefill, decode attention, and decode feed-forward computation stress those resources differently. Prefill is compute-intensive and sets time to first token (TTFT). Decode attention reads a growing key–value (KV) cache, and the feed-forward network (FFN) reads dense or expert weights, together setting time per output token (TPOT) [113], [117], [161], [162]. This mismatch creates two decisions. The *serving decomposition* chooses which roles get their own *pool* of accelerators. The *hardware assignment* selects an accelerator class for each pool. A *boundary* is where data crosses the network between pools. Prefill/decode disaggregation (P/D) separates prefill from decode; attention/feed-forward network disaggregation (AFD) splits decode attention from the FFN.

P/D is standard industry practice [23]. It is supported by serving frameworks such as NVIDIA Dynamo, vLLM, and SGLang [36], [126], [143]. AFD is also being seriously considered. ByteDance reports AFD in production on nearly 10,000 GPUs [162]. NVIDIA's Vera Rubin platform assigns decode attention to Rubin GPUs and mixture-of-experts (MoE) FFNs to Groq 3 LPX accelerators [14].

AFD adds a new serving boundary. Each boundary moves data, creates independently sized pools, can strand capacity, and restricts placement. AFD helps only if role-specific placement repays those costs. However, AFD sends each token across the boundary twice per MoE layer, or 116 times in DeepSeek-V3 [32]. In contrast, co-located decode with expert parallelism keeps expert communication within the decode pool, but the KV cache and expert weights share device memory. This can limit batch size as contexts grow [162]. Prior studies often change the boundary and hardware assignment together. Studying the two choices independently separates the effect of splitting decode from the effect of hardware assignment. Whether or not AFD becomes the preferred design, these decisions commit substantial capital, determine latency and throughput, and influence accelerator roadmaps. For accelerators still on the roadmap, hardware design changes become expensive once the silicon design is frozen [133]. We ask one question. *Does AFD repay its cost across future models and accelerators, and which lever matters more?*

To answer this question, we compare P/D and P/D+AFD and their hardware assignments before future models and accelerators are built. Existing AFD measurements come from system builders or hardware vendors, each using their own hardware and baseline [14], [43], [162]. However, a prospective comparison must account for future model demands, workload ranges, and changes in accelerator capabilities. We built SILICONFORGE, a calibrated cross-layer model that composes LLM architectures with hardware specifications. To build SILICONFORGE, we assemble a catalog of 39 accelerators in six hardware archetypes and define four classes for the comparison (Table I). Drawing on six published DeepSeek, Kimi, and Qwen models, we construct four prospective directions by varying expert and KV demands while rescaling width or depth (Table III). SILICONFORGE models compute and memory costs, communication, and pipeline overlap (§II-B–§II-C, §V-A). Queueing converts the resulting service times into goodput, while an event-driven simulation checks the queueing model. We calibrate against published measurements and check comparative accuracy on published comparison pairs (§V-B). SILICONFORGE reports several metrics, includ-

†Ramyad Hadidi wrote this paper independently, in personal time while at d-Matrix and at Volantis Semiconductor and in the interval between the two. The tools, code, and parameters contain no confidential information. All views are the author's own and do not represent those of any employer.

ing saturation throughput and service-level objective (SLO) goodput, the largest request arrival rate that meets both TTFT and TPOT targets [161].

Both designs share compute, memory, pipeline, and queueing models and a calibration policy fixed across the design space. Updating the models and calibration as future LLM and hardware specifications become clearer lets the community evaluate new designs. We independently optimize each design's mapping and pool sizes under a common power budget. A margin passes our two-part test only if its nominal magnitude exceeds the 9% envelope and its sign holds at every tested specification corner.

Our first finding is that **(I)** AFD has no robust deployment-level advantage in SLO goodput per kW across the accelerator classes and model directions in our main comparison. Most nominal estimates favor P/D. The largest AFD lead comes from fitting one more prefill replica into the budget. When decode alone is optimized, P/D+AFD has lower throughput per decode kW (§IV-A). Our second finding is that **(II)** AFD has a nominal lead in the KV-heavy model direction when the co-located expert pool spans several small scale-up domains. Larger domains or a fast fabric for both designs weaken that lead. More broadly, prefill provisioning, decode memory bandwidth, links, and pool granularity decide deployments more than the split alone (§IV-C). With decode mappings fixed, doubling memory bandwidth cuts TPOT by 39–49%, while doubling FLOPs cuts it by at most 1.8%. Prefill traffic also makes link bandwidth matter beyond the attention/FFN exchange (§IV-A, §IV-B). Our third finding is that **(III)** a fixed hardware assignment can lose its advantage as models, fabrics, hardware assumptions, and objectives change. Re-optimizing mappings and pool sizes on the same hardware cuts early commitment's median loss of normalized goodput from 36% to 9%. The tested reserves add less recovery (§IV-D).

We make three contributions. First, **SILICONFORGE, a cross-layer model**, compares independently optimized P/D and P/D+AFD under common modeling assumptions and a common power budget. We check comparative accuracy on held-out published pairs for each boundary and report failures (§V-B). Second, we identify **when splitting decode helps**, showing how prefill provisioning, decode memory bandwidth, links, scale-up domains, and pool granularity govern its modeled benefit (§IV-A, §IV-B). Third, we quantify **the goodput cost of early hardware commitment** and the recovery available from re-optimizing mappings and pool sizes (§IV-D).

II. DISAGGREGATED SERVING FOR LLMS

Disaggregated LLM serving assigns request work to separate pools of accelerator replicas with independently chosen hardware, size, and batching [113], [117], [161]. P/D places prefill and decode in separate pools. P/D+AFD further separates decode attention and FFN into distinct pools. This section explains SILICONFORGE's modeling and metrics.

A. Serving pools and boundaries

A serving boundary is a handoff between pools, determining which work shares hardware and which crosses the fabric. Unified serving keeps prefill and decode in one pool. Production systems limit interference with chunked prefill and decode priority [4]. P/D places the two phases in separate pools and transfers the completed prompt KV state once per request (the *KV handoff*) [113], [161]. A request's KV cache holds its *resident context*. The *capacity-bound batch* is the maximum number of requests whose weights and caches fit in usable memory and therefore shrinks as context grows.

In an MoE layer, each token activates k of E experts [129] (8 of 256 routed experts in DeepSeek-V3). Expert parallelism (EP) spreads experts over decode units, sending each token to its experts and back (in-pool dispatch and combine). P/D co-locates attention and FFN/expert work within the decode pool, sharing devices and a batch. P/D+AFD separates an attention pool that holds and reads KV state from a dense or expert FFN pool. Activations cross the *inter-pool link* twice per MoE layer of every decode step, once each way (the *exchange*) [150], [162]. Attention reads KV state, while experts repeatedly stream weights, creating different capacity and bandwidth demands. Role-specific placement can match them but adds recurring communication and idle capacity.

Figure 1 shows serving decomposition and hardware assignment as independent choices. Adding a boundary changes communication, pooling, capacity, and queueing even when the two pools it separates use the same accelerator class. Reassigning hardware changes service time, feasibility, and provisioned power without changing the boundary. We therefore vary the two axes separately. For each experiment, we fix the workload, precision, fabric, SLO, and queueing convention. A mapping sets tensor parallelism (TP), data parallelism (DP), EP, pipeline parallelism (PP), the per-replica batch, and the microbatch count M. For P/D and P/D+AFD separately, SILICONFORGE searches the allowed hardware assignments, mappings, and pool sizes (§III). It maximizes SLO goodput across feasible deployments under the common power budget.

B. LLM model demands on serving pools

LLM architecture determines which resources each pool consumes. Attention may be dense, sliding-window, or sparse, while its KV representation may use grouped-query attention (GQA), multi-query attention (MQA), or multi-head latent attention (MLA). FFN layers may be dense or MoE, with routed and shared experts. These choices change projection arithmetic, weight traffic, KV residency and read span, and the model state that must fit in each pool [21], [114]. In-

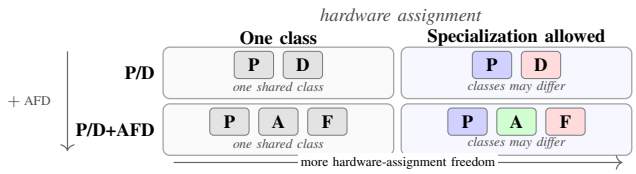


Fig. 1. **Serving decomposition and hardware assignment.** P, D, A, and F denote prefill, decode, attention, and FFN.

put sequence length (ISL), resident context, output sequence length (OSL), batch, and precision scale those demands. SILICONFORGE encodes the model through its layer, projection, attention, expert, context, and precision parameters. SILICONFORGE counts causal attention until a sliding window caps it, uses the declared GQA/MQA or MLA dimensions, activates top-k rather than all E routed experts, and accounts for shared experts separately. Each hardware entry supplies the corresponding compute, bandwidth, capacity, network, and nameplate-power parameters. SILICONFORGE derives compute and memory time from operator-level arithmetic and modeled memory traffic, then combines them with collective costs and frozen efficiency factors [53], [149]. SILICONFORGE models prefill as one service phase over the full prompt. Its residency check includes weights, prompt KV, and one chunk of activations in usable memory. For MoE decode, SILICONFORGE estimates attention and FFN service times separately and composes them with dispatch and combine costs. This demand–supply split lets SILICONFORGE evaluate specification ranges for hardware that does not yet exist [127]. For each pool, SILICONFORGE models FLOPs, bytes, state, feasibility, service time, and token throughput.

LLM architecture changes latency and feasibility through different paths. Dense attention makes KV residency and per-step reads grow with context, while sliding-window attention caps both. Sparse attention reduces selected-token reads but retains the full resident cache and index scan. Sparse attention can therefore reduce time without removing a capacity wall. GQA shards KV only through its supported head factor, whereas MLA KV remains replicated across tensor-parallel ranks. FFN service reads the dense-layer, routed-expert, and shared-expert weights used on each step. Uneven token routing can leave some expert-hosting units idle while the busiest unit finishes its work. This can lengthen FFN service and concentrate dispatch and combine traffic. SILICONFORGE uses mean routed load in the main comparison and evaluates expert imbalance as a sensitivity (§VI). SILICONFORGE charges every expert assigned to a unit against that unit's capacity. A pool is infeasible when its weights, KV state, and activations do not fit in usable memory. For feasible decode pools, SILICONFORGE combines compute and memory time with partial overlap, then adds collectives and fixed per-layer costs. SILICONFORGE allows decode microbatches to overlap, with pipeline fill and drain evaluated as a sensitivity (§V-D). SILICONFORGE streams every modeled weight and KV byte from each hardware entry's serving memory tier.

C. End-to-end serving metrics

TTFT includes prefill service (§II-B), the KV handoff, and waits for prefill and decode admission. The handoff transfers completed prompt KV state once per request and contributes to TTFT, not steady-state TPOT. We model it as store-and-forward without compression, prefix reuse, or layer-wise streaming.

TPOT depends on the recurring decode schedule. Figure 2 illustrates how overlap affects TPOT through several example decode schedules. The attention/FFN boundary exchanges activations twice per MoE layer of every decode step. It lengthens TPOT unless microbatch overlap hides the exchange. Co-located decode can hide its in-pool dispatch and combine with *two-batch overlap* (Figure 2a). One microbatch then communicates while the other computes [33], [138]. P/D+AFD hides the exchange with *ping-pong* pipelining of M microbatches between the pools [43], [162]. With M microbatches of b requests in flight, each resource serves the phases in one fixed order. TPOT is this schedule's steady *period* T, in which every resident request emits one token. For a homogeneous P/D+AFD stack ($M \le 8$) with a dedicated inter-pool link,

$$T = L \max\big(M \max(t_{\mathrm{A}}, t_{\mathrm{F}}, t_{\mathrm{D}}, t_{\mathrm{C}}),\ t_{\mathrm{A}} + t_{\mathrm{D}} + t_{\mathrm{F}} + t_{\mathrm{C}}\big), \quad (1)$$

where t_{A}, t_{D}, t_{F}, and t_{C} are one microbatch's attention, dispatch, FFN, and combine times in each of L layers. The busier pool sets T in Figure 2b and Figure 2d, hiding the exchange (§IV-B). In Figure 2c, the round trip $t_{\mathrm{A}}+t_{\mathrm{D}}+t_{\mathrm{F}}+t_{\mathrm{C}}$ sets T and exposes the exchange. A link can also set T. Max-plus algebra exactly evaluates this order for mixed dense and MoE stacks and co-located P/D ($M \le 2$). A shared link also carries the in-pool collectives. A design holds $U = Mb$ resident requests and delivers $X = U/T$ tokens/s. With $M = 1$, Eq. (1) is the submitted serial law. The fill-and-drain effect remains a sensitivity (§V-D).

SLO goodput is the largest request arrival rate satisfying both TTFT and TPOT targets and the stability constraint (§V-A). At each arrival rate, SILICONFORGE adds the modeled 99th-percentile (p99) of summed prefill and decode queue waits to base TTFT and tests these constraints. Pool separation can remove interference and enable role-specific batching, but it adds queues and caps SLO goodput at that of the least-

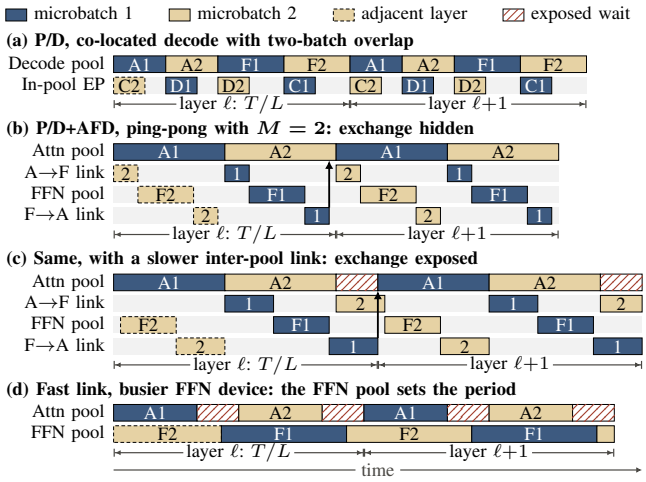


Fig. 2. **Microbatch overlap hides the attention/FFN exchange only when the busier pool sets the steady-state period.** Steady-state decode schedules over two layers with $M = 2$ microbatches. A, D, F, C: attention, dispatch, FFN, combine. Arrows mark microbatch 1's return. (a) Co-located decode hides D and C. (b) AFD ping-pong hides the exchange in the slack of the shorter FFN stage. Balanced stages need $M \ge 3$ (§IV-B). (c) A slower link's round trip outlasts both microbatches' attention; the attention pool idles. (d) A busier FFN device lengthens F to set the period; attention waits. Routed tokens can crowd one device's experts.

TABLE I
HARDWARE CATALOG AND STUDY ROLES: 39 ACCELERATORS IN SIX ARCHETYPES.

Hardware archetype (entries)	Catalog entries by release status (unmarked: current; *Ann.*: announced, pre-release; *Spec.*: speculative, projected specifications)	Role in this paper
GPU (13)	A100 [93]; H100/H200 [27], [95]; B200/GB200/GB200 NVL72 [94], [139]; AMD MI300X/MI325X/MI355X [10]. *Ann.:* B100 [139]; GB300 [98]; Rubin [105]; Rubin Ultra [106].	GPU class (Rubin anchor)
Custom HBM (11)	Inferentia2 [8]; Trainium2 [9]; TPU v5e/v5p/v6e [45]–[47]; TPU v7 Ironwood [48]; Gaudi 3 [55]; Maia 100 [80]; RNGD [44]; ATOM [123]. *Ann.:* REBEL [124].	Systolic class (TPU v7 anchor)
3D-DRAM/in-memory (2)	*Ann.:* d-Matrix Raptor [89]. *Spec.:* Fractile Transformer Chip [42].	3D-DRAM class (Raptor anchor)
SRAM/dataflow (5)	Cerebras WSE-3 [20]; Groq LPU v1 [1]; SambaNova SN40L [116]; Untether speedAI240 [141]. *Ann.:* Groq 3 LPX [14].	SRAM/dataflow class (Groq 3 LPX anchor)
Commodity DRAM (5)	MTIA v1/v2 [77], [78]; Tenstorrent Blackhole/Wormhole [134], [135]. *Ann.:* Positron Asimov [115].	Tool support (Figure 3)
Model-specific ASIC (3)	*Spec.:* Etched Sohu [87]; MatX C1 [76]; Taalas HC1 [88].	Tool support (Figure 3)

TABLE II
PROSPECTIVE ACCELERATOR CLASSES MODELED IN THIS STUDY. VALUES ARE NOMINAL PER DEPLOYMENT UNIT [LOWEST–HIGHEST SPECIFICATION CORNER]. ACROSS CLASSES, NOMINAL VALUES SPAN LESS THAN 2× IN COMPUTE, 163× IN MEMORY BANDWIDTH, AND 72× IN CAPACITY.

Class (anchor, memory)	Unit	Tier[1]	FP8 PFLOPS[2]	Mem. TB/s	Cap. GiB	Scale-up TB/s	Domain	Scale-out Tb/s	Power W (est.)[3]
GPU: Rubin[4] [102], [105], HBM4	2-die package	Ann. 1.25	17.5 [17.5–37.2]	19.2 [19.2–30.0]	288 [288–450]	1.5 [1.5–2.3]	72	1.6 [1.6–2.5]	1,800 [1,665–2,475]
Systolic[5]: TPU v7 [48], HBM3e	2-die chip	Datash. 1.0	13.8 [9.2–18.5]	7.4 [7.4–11.1]	192 [192–288]	0.6 [0.6–0.9]	9,216	0.10 [0.10–0.15]	600 [555–825]
3D-DRAM: Raptor [89]	2-chip card	Est. 1.5	10.0 [10.0–16.3]	100 [100–225]	32 [32–152]	1.0 [1.0–1.6]	8	0.8 [0.8–1.3][6]	844 [591–1,097]
SRAM/dataflow: Groq 3 LPX [14]	8-LPU tray	Ann. 1.25	9.6 [9.6–20.4]	1,200 [1,200–2,550]	4.0 [4.0–17.5]	10.0 [10.0–21.3]	32	0.8 [0.8–1.7][6]	3,000 [2,100–3,900]

Electrical fabric: Class tiers as above, per direction and unit (vendor bidirectional figures halved). Per-hop latency is 0.5–2 µs on scale-up tiers and an estimated 4 µs on scale-out, with 4–8 µs as a sensitivity [51]. A cross-class inter-pool link runs at the slower endpoint's scale-out rate (systolic data-center network, DCN: 0.1 Tb/s = 12.5 GB/s).
Photonic fabric: At nominal specifications, every inter-unit tier both designs use runs at no less than 12 Tb/s per direction [4–32], with latency as electrical. Public optical I/O parts deliver 8–64 Tb/s (both directions) per engine [15], [69] and 114 Tb/s per interposer [70].
[1]Confidence and range-widening factor; Datash.: datasheet; Ann.: announced; Est.: estimated. [2]Dense peaks where published. [3]Nameplate, without hosts, switches, or cooling. [4]Rubin HBM and NVLink values differ across NVIDIA sources [13], [104], [105]. The range covers both. [5]Constructed from the TPU v7 memory system with 2–4× its 4.6 PFLOPS (3× nominal; not widened). [6]Estimate. 3D-DRAM also uses a PCIe 7 rack scale-up tier at 0.256 TB/s per direction, with an estimated 64-card domain.

admissible pool. SILICONFORGE returns SLO goodput and the *saturation throughput* of the complete deployment, its largest sustainable token rate. A design can gain throughput yet lose goodput by lengthening TPOT near a tight target. We therefore report both and vary the target (§IV-C). By default, both designs use the same nameplate power ceiling. We report goodput per kW using the selected hardware's summed rated power, reflecting how many accelerators a power-capped rack may admit [38], [112]. Decode-only comparisons use decode kW. We also normalize goodput by *deployment unit*, the smallest unit a vendor ships (§III-B). We include only mechanisms with explicit cost models and call one deployment better only when its margin passes the two-part test (§V-C).

III. EVALUATION SCENARIOS

A. Serving decomposition and hardware assignment

Our main comparison evaluates the incremental attention/FFN split by comparing **P/D** with **P/D+AFD** (Figure 1). Unified serving is considered separately in the KV-footprint sensitivity (§IV-C), where its modeled SLO goodput is an upper bound because chunked prefill is hidden in decode steps. A *placement policy* constrains hardware assignment by specifying which pools may use different accelerator classes. **One-class placement** uses one class for every role and compares homogeneous deployments. **Phase-split** lets prefill and decode differ. **Role-specific** lets prefill, attention, and FFN differ. **FFN-targeted** holds prefill and attention on one class and chooses the FFN class freely.

B. Four accelerator classes expose different resource tradeoffs

SILICONFORGE's hardware catalog contains 39 accelerators across six archetypes, with current, announced, and speculative entries (Table I). Archetypes group hardware by organization. Table I lists the accelerators, their release status, and their study roles. Commodity DRAM and model-specific ASIC appear in the catalog sweep but not the main comparison.

Using accelerator anchors from Table I, we define four prospective classes for the main comparison: GPU, systolic, 3D-DRAM, and SRAM/dataflow. These classes span different resource tradeoffs because accelerator roadmaps do not scale compute, memory bandwidth, and capacity together [14], [29], [48], [105]. TPU v7's memory system anchors the constructed systolic class, although Table I groups that accelerator under Custom HBM. SILICONFORGE models each class's resources as *ranges* to test comparisons across uncertainty in published and estimated specifications. Table II lists the nominal resource values and declared ranges for each class. The 32 *specification corners* (64 with the photonic band) combine endpoints of compute, memory bandwidth, capacity, links, and power. At each corner, we optimize each design's allowed hardware assignments, mappings, and pool sizes for maximum SLO goodput within the common power budget. For each resource, all classes use their own lower or upper endpoint together. Lower-confidence inputs use wider ranges, and no capability corner falls below its anchor. A range-width curve scales every widening factor from $0.5\times$ to $2\times$.

Figure 3 illustrates SILICONFORGE's mapping coverage across the full hardware catalog for DeepSeek-V3 with ISL and OSL both 16K. The sweep uses one-class placement for decode attention and FFN, with ceilings of 128 units and 1 MW. It varies the hardware system, release status, mapping (TP, DP, EP, batch, and $M \leq 8$), and deployment size. Moving right means faster token deliv-

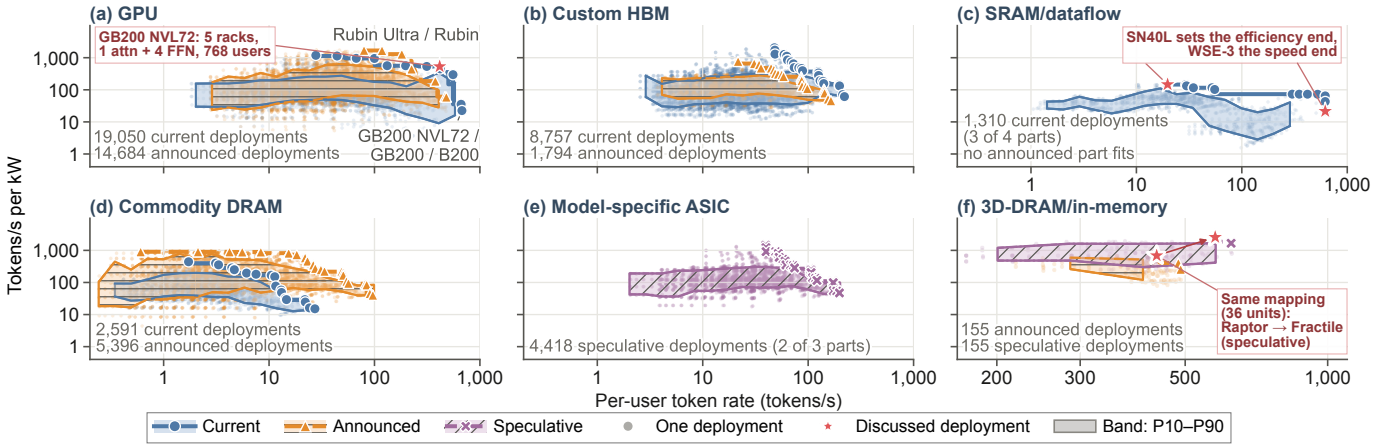


Fig. 3. **Coverage of the hardware catalog under one controlled workload.** (a)–(f) Six archetypes; DeepSeek-V3 deployments with ISL and OSL both 16K, one-class placement for decode attention and FFN, $\leq$128 units, and $\leq$1 MW; 36 of 39 accelerators support at least one of the 58,310 feasible deployments. Parts without native FP8 run FP8-stored weights at their 16-bit rate. Bands: P10–P90 of deployments; Figure 3f has its own x range.

TABLE III

PROSPECTIVE DIRECTIONS AND MODEL CATALOG. THE FOUR DIRECTIONS SPAN 35–55B ACTIVE PARAMETERS (1.6×). TOTAL WEIGHTS VARY BY 5.6×, AND STORED KV PER TOKEN VARIES BY 8.9×. THE DIRECTIONS USE C = 8K/32K/128K (ISL = C, OSL = 1,024, FP8). KV PER REQUEST IS KV PER TOKEN $\times(C+\text{OSL})$. A STEP READS KV PER TOKEN $\times\, C$. SPARSE ATTENTION INSTEAD READS THE TOP-2,048 TOKENS PLUS THE FULL INDEX.

(a)	**Four prospective model directions (nominal)**			
Demand varied	**Expert-heavy MoE** **FFN work, expert capacity**	**KV-optimized MLA** **KV bytes per token**	**KV-heavy GQA-MoE** **KV-cache capacity**	**Sparse-attention MLA** **KV reads per step**
Anchor (total/active)	Kimi K2 [61] (1.04T/32B)	DeepSeek-V3 [32] (671B/37B)	Qwen3-235B [120] (235B/22B)	DeepSeek-V3.2-Exp [34] (685B/37B)
Trend from (published models)	3: DeepSeek-V2, V3, Kimi K2 [31], [32], [61]: experts 160→256→384, active share 8.9→5.5→3.1%	4: DeepSeek-V2, V3, R1, Kimi K2 [31], [32], [49], [61]: latent rank 512 in all four; a what-if	1: Qwen3-235B's 96 kB/token FP8 GQA cache; the size range is a scenario	1: V3.2-Exp sparse attention [34], [157]: top-2,048 tokens, 128-wide index
Construction	Experts ×3, width ×1.2, expert FFN ×1.125; active share 1.0%	Latent rank 512→320, width ×1.1	Width ×1.31, depth ×1.73 (94→163 layers), every layer MoE	Width ×1.1; budget and index fixed
Total / active params	4.11T / 42B	737B / 35B	916B / 55B	737B / 35B
Layers / MoE layers	61 / 60	61 / 58	163 / 163	61 / 58
Experts rt./sh./top-k	1,152 / 1 / 8	256 / 1 / 8	168 / 0 / 8	256 / 1 / 8
Width / query heads	8,576 / 64	7,936 / 64	5,376 / 40 (5 KV)	7,936 / 64
KV per token (kB)	35.1	23.4	208.6	42.9 (35.1 + index 7.8)
(b) Family	**Catalog**: 20 published model anchors plus one scaled proxy		Role in the study	
Dense transformer (6)	Llama-3.1 8B/70B/405B [73]; Mistral 7B; OPT-13B; Qwen2.5-72B		Calibration and controls; no synthetic dense growth point	
MoE with GQA (9)	Mixtral 8x7B/8x22B [56]; Qwen3 30B/235B; Llama 4 Scout/Maverick; GPT-OSS 20B/120B [110]; Grok-1		Uncompressed GQA KV; Qwen3-235B seeds the KV-heavy direction	
MoE with MLA (5+1)	DeepSeek-V2/V3/R1/V3.2-Exp; Kimi K2; scaled 2T MoE proxy		Latent KV; seeds the other three directions	

ery to each user; moving up means more throughput per kW. Each frontier traces feasible mapping and deployment choices. The GB200 NVL72 star in Figure 3a marks a balanced deployment with 4× as many FFN racks as attention racks. Points farther right trade throughput per kW for faster token delivery by serving fewer users. Figure 3b covers custom-HBM accelerators. In Figure 3c, SN40L sets the efficiency end of the current SRAM/dataflow frontier, and WSE-3 sets the speed end. The preferred system depends on the deployment target. Figure 3d and Figure 3e cover commodity-DRAM and model-specific ASIC accelerators, respectively. Groq 3 LPX and Groq LPU v1 in Figure 3c cannot hold the model in 128 units, and Taalas HC1 in Figure 3e targets another model. The matched mapping in Figure 3f predicts 3.7× Raptor's throughput per kW for Fractile, using projected Fractile and announced Raptor specifications.

C. Communication fabrics and collectives

Optical fabrics are maturing across the interconnect hierarchy [15], [71], [96]. We model electrical links as the current baseline and use the photonic roadmap range listed in Table II for sensitivity analysis. SILICONFORGE represents each fabric as a hierarchy of link tiers defined by bandwidth, latency, and supported group size. Within each fabric, we compare a dedicated inter-pool link with a shared scale-up domain, where the attention/FFN exchange competes with in-pool collectives (e.g., local TP reduction [102]). A faster inter-pool link shortens AFD's exchange, but the same upgrade in a shared domain also accelerates P/D's in-pool collectives. We evaluate fabric and serving choices jointly under both modes.

Data movement and synchronization can erase the throughput benefit of additional TP, PP, DP, or EP [64], [90], [114], [130]. SILICONFORGE derives message sizes from the model, mapping, and precision, and sizes DP replicas. It charges the expert all-to-all per hop on the tier that hop crosses (§V-A) and every other collective on the tier that spans its participants. SILICONFORGE models in-network collective reduction only when the selected fabric supports it (e.g., SHARP [103]). Otherwise, it uses recursive halving/doubling (Rabenseifner), with ring and offload-disabled implementations as sensitivities.

D. LLM architecture directions

SILICONFORGE evaluates specific LLM models and controlled future directions. These vary model properties separately rather than along one "model size," following recent frontier families that move expert width, attention state, and context on separate axes [35], [63], [86], [121]. Expert-heavy MoE increases FFN work and expert communication while activating only a fraction of its weights [39], [64], [129]. Total weight capacity and active compute can therefore grow differently. Attention variants, from GQA [5] to MLA [31], change the KV bytes stored per token. Longer contexts make this state a capacity and data-movement constraint [62], [117], [156]. Sparse attention reduces selected KV reads per step while retaining the complete cache [34], [75], [157]. A model can read little KV yet exceed attention-pool capacity.

The model catalog contains 26 entries, including 25 published model anchors and one scaled 2T MoE proxy. Table III(b) lists 20 of these anchors and the proxy. The main comparison uses four controlled future directions rather than averaging across the catalog. Each compound synthetic scenario extends one model family mainly along one demand dimension [28] while rescaling width or depth, as shown in Table III(a). Their resident contexts are $C = 8$K, 32K, and 128K with ISL $= C$. Model mechanisms enter through KV bytes per token and bytes read per step. Gated attention adds no KV state [119]. A hybrid with full attention in a fraction f of layers, such as Qwen3.5 ($f = 1/4$) [121], stores about f times the KV per token plus a fixed state per request. That storage sets its capacity need.

E. SLOs, goodput, workload, and budget

SILICONFORGE sweeps the request arrival rate to test both latency targets (§V-A). In the main sweep, TPOT is fixed at each deployment's full-occupancy value, while queueing raises tail TTFT until its target fails. The separate load simulation lets TPOT vary with batch occupancy (Figure 8). Each comparison *cell* fixes one model direction, fabric, link-sharing mode, context, and placement policy. Its SLO pairs a TTFT target of 1 or 5 s with a TPOT target of 10, 20, 50, or 200 ms. The separate regime map sweeps eight contexts (4K–256K) and 24 TPOT targets (10–300 ms) at nominal specifications. In the main workload, the prompt fills the resident context (ISL $= C$), and the KV handoff moves C tokens. Each request produces 1,024 output tokens and has no prefix-cache hit. Every policy uses a 128 kW budget. Scale runs use 512 kW. One-class placement is also evaluated at 64 units. Under the main search rule, EP starts at 8 and doubles for both designs. We sweep $M = 1, \ldots, 8$ for P/D+AFD and $M = 1, 2$ for P/D. Prefill TP exceeds 8 only if no smaller replica fits.

The 16 *headline comparisons* cross four directions, two fabrics, and two link-sharing modes. Each uses $C = 32$K, a 50 ms TPOT target, a 5 s TTFT target, a 128 kW budget, and FP8 weights, KV, and activations, except 16-bit combine. We define two verdict sets before presenting the results (§V-C). The *best-allowed* set represents the architect's decision and gives each design its best allowed placement policy. The *one-class* set gives each design its best single class. Both designs select the same class in 14 of the 16 comparisons.

IV. WHEN DOES SPLITTING DECODE PAY?

We vary the serving decomposition and hardware assignment independently, in four steps. Does adding the attention/FFN boundary help under a common budget? Which parts of decoded-token latency, and which link, determine whether role-specific placement repays that boundary? When a fixed deployment exceeds capacity, which lever restores feasibility? Which hardware assignments remain stable as the model, fabric, hardware assumptions, and objective change?

A. Under one budget, the ranking depends on pool allocation

Does the attention/FFN split help by itself, or through different accelerator classes? Figure 4 compares the four model directions relative to P/D's SLO goodput per kW at 100%. AFD− (Step 1) compares each design's best one-class deployment. AFD+ (Step 2) allows role-specific placement for P/D+AFD and phase-split placement for P/D. Circles mark electrical cases and squares photonic. Solid and dashed blue segments lead to AFD− and AFD+, respectively. The gray band marks the 9% envelope around P/D. Whiskers show AFD+ with finer P/D decode pool sizes.

Each comparison independently searches both designs' mappings and pool sizes for the highest feasible SLO goodput under 128 kW, reported per kW. Workload, SLO, precision, calibration, and available classes stay fixed. Each comparison uses its own optimized P/D reference. At nominal values, the AFD− comparison has no consistent winner. Role-specific placement in AFD+ changes little. Under the main power-of-two EP rule, only photonic sparse attention lies beyond the 9% envelope (favoring P/D), and none is robust over the tested specification corners (§V-D).

The extra class choices in AFD+ change the margin in only four of eight cases. GPU placement helps P/D+AFD through the FFN pool in expert-heavy MoE and through prefill in KV-heavy electrical. For example, expert-heavy MoE on photonic fabric selects a GPU FFN pool under AFD+. Its margin improves by 5.8 points (Figure 4a). P/D also benefits from phase-split placement, which moves the KV-optimized photonic comparison toward P/D (Figure 4b). Extra class choices can improve either design.

Pool allocation explains the positive headline margins. When optimized alone under the same TPOT target, P/D has higher throughput per decode kW in every cell. Selected best-allowed P/D+AFD deployments also have longer TPOT than P/D, although both meet the target. KV-heavy GQA-MoE on photonic fabric gives the largest P/D+AFD margin, +8.1% (Figure 4c). Its pool allocation leaves room for eleven prefill replicas, versus ten for P/D. That replica explains the gain.

At the headline workload, sharing the attention/FFN link with in-pool collectives (e.g., local TP reduction) does not limit the selected deployments. Dedicated and shared modes select the same configurations and yield the same margins,

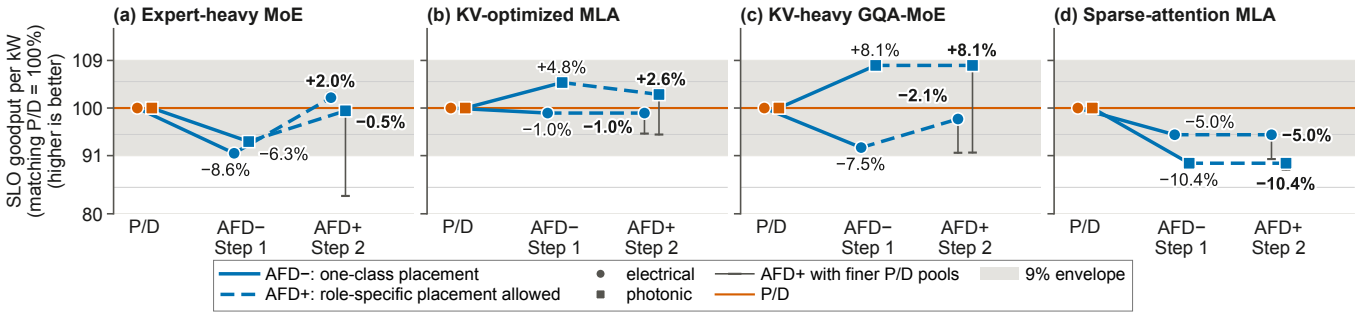


Fig. 4. **Under the revised model and 128 kW, adding the attention/FFN boundary on one class moves SLO goodput per kW by -10.4% to $+8.1\%$, and role-specific placement changes little. Seven of eight AFD+ margins lie inside the 9% envelope.** (a)–(d) Headline cells (32K, TPOT 50 ms, TTFT 5 s, dedicated). Whiskers allow any integer EP for P/D (-16.6% to $+2.9\%$ under AFD+).

giving eight distinct results from 16 comparisons. At nominal values, the search selects systolic and GPU classes. Keeping all FFN weights resident on the modeled SRAM/dataflow class exceeds the 128 kW budget for these directions.

FastAFD measures 1.35–1.45× the per-GPU decode throughput of tuned co-located vLLM [43]. AFD-Ledger's model re-provisions both designs under one budget and narrows AFD's Qwen3-235B 8K gain to 0.99× [118]. On these development data, SILICONFORGE predicts 1.37× and 1.47× at FastAFD's recorded 8K and 16K deployments. Optimizing each design within FastAFD's GPU budgets gives 0.94× at both. In these modeled cases, AFD's gain disappears when both designs can optimize their mappings and pool sizes under the same GPU budget.

Finer EP choices can avoid oversized decode pools, leaving more power for prefill. The main power-of-two rule makes P/D resize its co-located decode pool in larger steps, while P/D+AFD can size attention separately. Allowing any integer EP for P/D (fractional experts per rank, §V-A) removes most P/D+AFD regime-map leads beyond 9% (§IV-C). This relaxes only P/D's sizing rule. Giving both finer pool sizes restores some leads in the tested regime-map cases, but no nominal headline P/D+AFD margin exceeds 9%. Starting EP below 8 has little effect at the headline workload. With finer sizing for both designs, most surviving leads reflect lower power at nearly the same absolute goodput, and a few improve it.

Takeaway 1. Headline margins lean P/D and depend on pool allocation, search limits, and prefill assumptions. They establish no robust deployment-level AFD advantage over P/D.

B. Role-specific placement trades weight reads for exchange

Why does faster FFN hardware sometimes leave TPOT unchanged? Figure 5 shows how TPOT changes with context for the four model directions, holding each direction's selected P/D deployment and batch size fixed. The upper strip shows TPOT by component in milliseconds, and the lower stack shows component shares. The gray region marks where that fixed batch no longer fits in memory.

Weight-read time stays nearly constant per step, whereas KV work grows with context. Memory reads take 57–95% of TPOT in these deployments. For example, KV reads overtake weight reads at about 5K tokens in the KV-heavy model direction (Figure 5c). Faster FFN weight reads then address a shrinking share of decode time. Sparse attention caps selected-token reads, but its index scan and full resident cache still grow (Figure 5d). All four fixed deployments run out of capacity before TPOT reaches the 50 ms target. Longer contexts require re-batching or another deployment, evaluated in §IV-C.

As Figure 2b illustrates, faster FFN weight reads leave TPOT unchanged when attention remains the bottleneck. For this run, Figure 6a starts from the one-class P/D+AFD deployment selected for each model–fabric case. The baseline search varies batch size and $M = 1, \ldots, 8$ along with hardware, mappings, and pool sizes. We then move only the FFN pool to the GPU class, keeping attention, prefill, the selected batch size and M, mappings, and pool sizes fixed. Pale bars show time absorbed by overlap. Dark bars show time that changes TPOT, and diamonds give the net change. For KV-optimized MLA on electrical fabric, three microbatches keep attention busy.

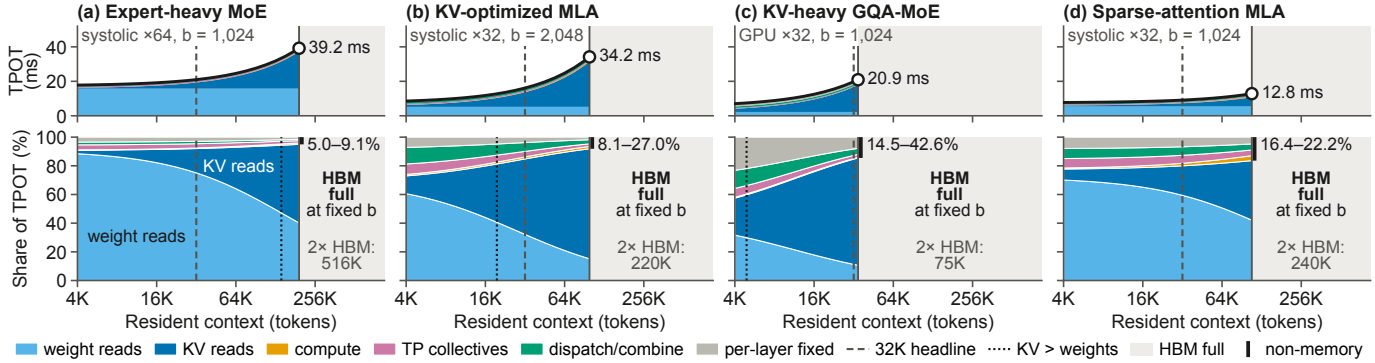


Fig. 5. **Context shifts decoded-token time from weight reads toward KV work while absolute latency rises.** (a)–(d) Each panel fixes one direction's selected P/D deployment (headline cell, electrical; decode class, units, and batch b printed) and grows the resident context. Top: TPOT by component; bottom: exact additive shares (one microbatch). Gray zone: past the wall, b exceeds the capacity-bound batch (label: wall at 2× HBM capacity); re-batching serves longer contexts (Figure 10). Bar: non-memory share at the wall (label: range).

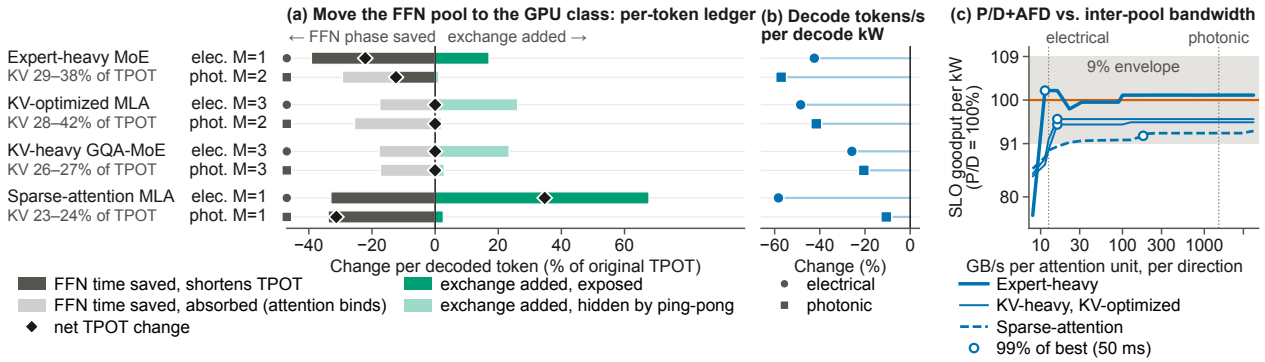


Fig. 6. **Moving the FFN pool to GPUs saves FFN time equal to 17–39% of original TPOT, yet every move loses decode tokens/s per decode kW.** Baselines in Figure 6a–b are one-class P/D+AFD deployments selected under 128 kW at 32K context, a 50 ms TPOT target, and a dedicated link. (a) Only FFN hardware changes. Row labels give this run's selected M, held fixed with batch size. Ledger in % of original TPOT; KV-read time is unchanged. (b) Change in decode tokens/s per decode kW; reassignment changes power. Circles mark electrical and squares photonic. (c) Separate cross-class searches relative to P/D at a 50 ms TPOT target (electrical, catalog domains, 4 µs). Circles mark 99% of each direction's best goodput. Dotted lines mark the links in Figure 6a–b.

The reduction in FFN service time equals 18% of original TPOT. Added exchange equals 26% of original TPOT, yet TPOT is unchanged. In this run, the selected sparse electrical deployment uses one microbatch. Without overlap, its TPOT grows by 35% after the FFN move. In three other moves, TPOT falls. However, Figure 6b shows that all eight moves reduce decode tokens/s per decode kW after accounting for the higher decode power of GPU reassignment. Shorter FFN service alone does not establish a more efficient deployment.

Inter-pool bandwidth helps until exchange no longer delays decode. For a homogeneous P/D+AFD stack on a dedicated link, hiding the exchange requires two conditions from Eq. (1). A microbatch's full round trip must finish within the busier pool's work on all M microbatches, and neither transfer may outlast that pool's work on one microbatch. Figure 2b meets these conditions, but Figure 2c does not. Unequal stages can leave enough slack with $M = 2$, whereas balanced stages need at least three microbatches. At fixed microbatch size, extra microbatches keep more KV state resident. Fitting that state while still meeting the TPOT target can require more devices or smaller microbatches. With one microbatch, the selected sparse-attention deployments expose the round trip and leave both pools below 60% utilization.

In Figure 6a, every $M \geq 2$ move already hides its exchange on its existing link. Figure 6c shows what more bandwidth would buy. A separate search over cross-class P/D+AFD deployments sweeps the inter-pool bandwidth and reports SLO goodput per kW relative to P/D. Three of four model directions reach 99% of their best goodput at 11–16 GB/s per attention unit, per link direction (circles; 50 ms TPOT target, catalog scale-up domains). Beyond this knee, extra bandwidth adds little goodput. Sparse attention gains only about 3% more. At this 50 ms target, no swept link produces a P/D+AFD lead beyond 9%. At a tighter 10 ms TPOT target, expert-heavy's nominal lead over its optimized P/D reference is 17.2% at 8–200 GB/s (not shown). That lead falls to 3.8% with finer P/D pools. Hiding the exchange removes a cost but does not guarantee a deployment-level win [68].

In 8-unit scale-up domains (one 8-GPU server), the KV-heavy P/D decode pool spans several domains at 32K context and a 50 ms TPOT target. Expert traffic across domains delays decode. P/D+AFD keeps its FFN pool in one domain. Its nominal lead is 9.2%, falling to 2.8% with finer P/D pools. No specification corners were tested. Larger domains or sufficiently fast links for both designs cut the lead below 9%.

With the decode mappings of the 64 selected headline deployments (16 comparisons × two designs × two verdict sets) fixed, doubling memory bandwidth cuts TPOT by 39–49%, versus at most 1.8% for doubling FLOPs. Complete deployments can favor different upgrades because prefill also needs compute and pays for all-reduce and KV handoff. With uncached prompts, prefill uses 38–85% of these deployments' power. Re-optimizing each design's hardware assignments, mappings, and pool sizes under 128 kW can therefore make compute or link upgrades improve SLO goodput even when fixed decode barely responds.

Takeaway 2. FFN savings reduce TPOT when they shorten the limiting stage or round trip. Faster decode alone does not establish higher SLO goodput per kW, because prefill and power can change which upgrade helps.

C. Re-batching or reassignment restores feasibility

When context or arrival rate makes a fixed deployment infeasible, is the serving boundary at fault, or has one mapping exhausted its resources? We vary context, TPOT target, arrival rate, and KV footprint, then search offline for changes that restore feasibility. Figure 7 maps the margin for the four model directions over resident context (horizontal) and TPOT target (vertical). Diagonal hatching marks margins inside ±9%, and vertical hatching marks P/D+AFD leads beyond it. The plus marks the 32K, 50 ms headline cell. Dots mark leads beyond the envelope only with power-of-two P/D pools. P/D's leads beyond 9% (unhatched) cluster at TPOT targets of 31 ms or tighter and are largest in Figure 7a and Figure 7c. Prefill replicas and rounded pool sizes change in steps as context grows, shifting the margin. Context alone therefore does not give a single threshold for choosing the serving boundary.

We next separate throughput limits from latency-target failure. At P/D's largest headline lead, Figure 8a–c plots throughput, p99 TTFT, and p99 TPOT against arrival rate. P/D+AFD's absolute goodput and saturation throughput are

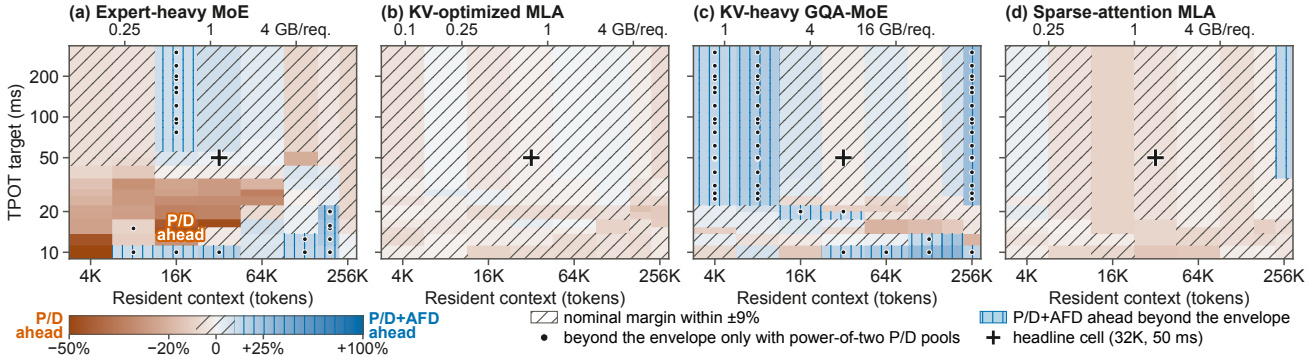


Fig. 7. **Co-optimized at 128 kW, P/D+AFD and P/D stay within the 9% envelope in 579 of 768 cells; finer P/D pools preserve 18 of 101 P/D+AFD leads beyond it and 86 of 88 P/D leads.** Margin: best P/D+AFD over best P/D in SLO goodput per kW (nominal specifications; electrical, dedicated, TTFT 5 s). Hatching: diagonal, within ±9%; vertical, P/D+AFD ahead beyond it. Top: KV per request. +: headline cell (32K, 50 ms); dots: beyond the envelope only with power-of-two P/D pools.

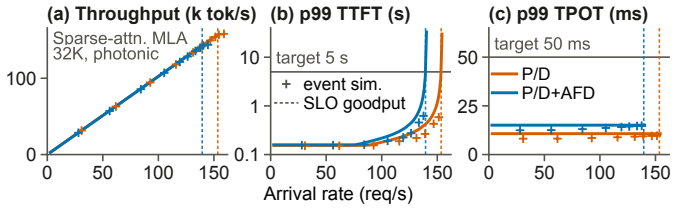


Fig. 8. **At P/D's largest headline lead, P/D+AFD's 9.1% lower absolute goodput comes from lower saturation throughput rather than different losses at the latency target. Both designs deliver 99% of saturation throughput within the SLO.**

both 9.1% lower; both designs deliver 99% of saturation within the SLO. TTFT exceeds its target near saturation while TPOT stays below its target, so the goodput gap reflects lower saturation throughput. In Figure 9, we vary KV heads in the KV-heavy model direction, re-optimizing both designs on GPUs at 32K under 128 kW. In Figure 9a, KV heads fall left to right from 40 (multi-head attention, MHA) to one (MQA) [128]. Each exit is SLO goodput; shading between the main curves marks rates where only the higher design meets both latency targets. Smaller caches cut per-request KV reads and storage, raising both load limits.

The thin P/D line allows finer decode-pool sizes, avoiding the main rule's coarse allocation steps. At MHA, P/D+AFD exits 45% above main P/D but 24% below P/D with finer pools. Only P/D receives this relaxation. The thin line exceeds P/D+AFD throughout the MHA-to-MQA sweep. Figure 9b shows both main configurations reaching 90–99% of saturation. Their goodput gaps mainly reflect different saturation throughputs. The MLA diamonds represent a separate model that also changes attention computation. Unified serving, not drawn, reaches up to 2.6× the best split design's goodput. This is an upper bound because chunked prefill is fully hidden in decode steps (§III-A).

The rescue search tests whether re-batching, remapping, or hardware reassignment restores feasibility as context grows. Remapping changes mappings and pool sizes on the same classes, whereas reassignment can replace classes that miss TTFT. Figure 10a–d plots resident context horizontally and the minimum provisioned power (kW) satisfying memory and SLO constraints vertically. Bars mark each 32K headline deployment's fixed, re-batched, and re-optimized limits. The last allows reassignment. Curves show the co-optimized power requirement. For example, the KV-heavy one-class P/D+AFD deployment (Figure 10c) stops at 34K because its batch no longer fits in memory. Re-batching, a new batch and M on the same pools, extends service to 168K. Full co-optimization extends both designs to 423K within 128 kW. With uncached prompts, prefill eventually limits both designs at the same context within each direction. The KV-heavy example reaches this TTFT wall even though attention capacity holds to 1M. The 5 s TTFT target becomes binding under our prefill rule (TP≤8 unless nothing smaller fits). Allowing prefill TP up to 64 makes 512K feasible for three directions.

Restoring feasibility does not restore 32K goodput. Figure 10e sweeps the budget for sparse attention at 256K, where power raises both designs' goodput. Figure 10f plots the best goodput at each context and budget as a fraction of the 32K best at 128 kW. At 256K, increasing sparse attention's budget from 128 to 512 kW raises that fraction from 1.3% to 9%. Per-request prefill time grows faster than context length.

The uncached-prompt wall does not apply unchanged to a cached prefix. We re-evaluate Wu et al.'s Qwen3-235B case with a cached 1M-token prefix (FP8 KV) [150]. Only the 4,096 new tokens are prefilled. Under the same capacity and

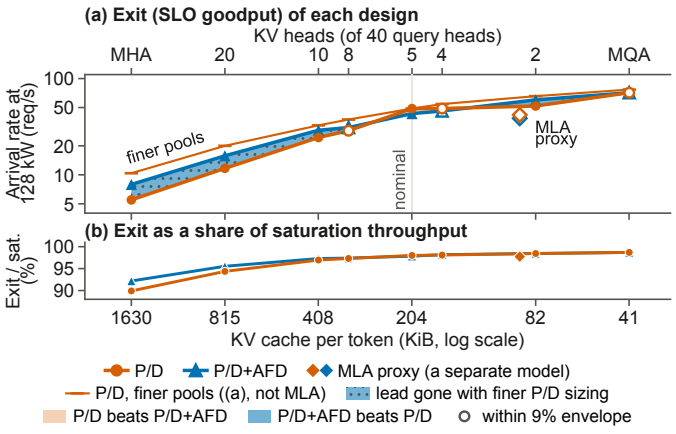


Fig. 9. **Smaller KV caches raise both designs' SLO goodput; finer P/D pools erase the P/D+AFD leads in the MHA-to-MQA sweep.** (a) Exits at TTFT 5 s and TPOT 50 ms, co-optimized on the GPU class under 128 kW (KV-heavy GQA-MoE, 32K). Main curves use power-of-two EP; the thin line uses finer P/D pool sizing. (b) Main-rule exit over saturation throughput.

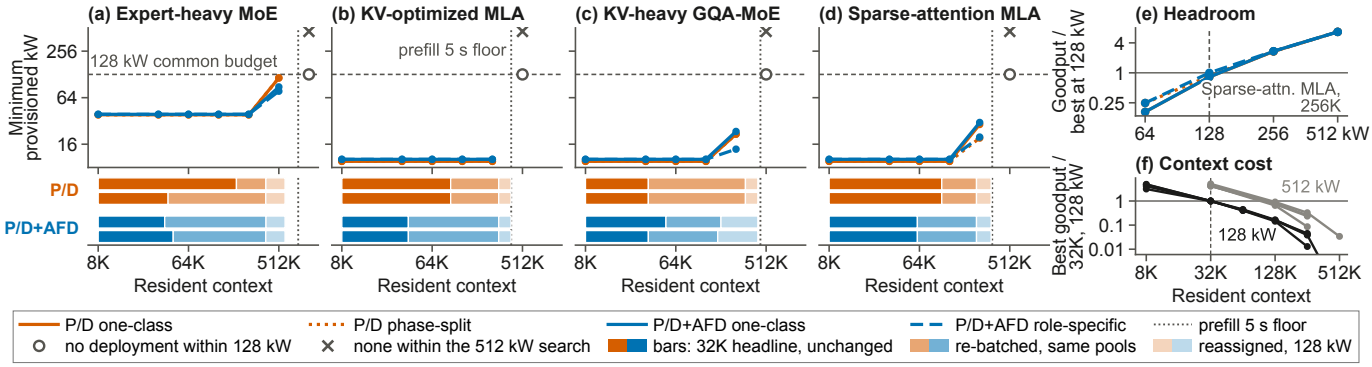


Fig. 10. **Re-batching or reassignment rescues every 32K headline deployment until both designs reach a TTFT wall at the same context.** (a)–(d) Upper bars: best-allowed; reassignment stays within 128 kW. Rescue does not restore short-context goodput. (e) Budget: sparse-attention MLA at 256K, P/D+AFD's largest 128 kW lead surviving finer P/D pools; 64-way prefill TP removes it. (f) Best goodput at 128 and 512 kW over the 32K best at 128 kW, for four directions.

performance rules for both designs, P/D fits on their B200. With our classes at 128 kW, it also fits at nominal values and all 32 corners. Their "AFD required" conclusion therefore does not follow. Under the main EP rule at 128 kW, best-allowed P/D+AFD leads at nominal values (+32%) and at all 32 corners (+5% to +99%). This lead is conditional (§V-C).

Takeaway 3. Context length alone does not choose the serving boundary. KV footprint, latency targets, and pool sizing shape both designs' supported load. Re-optimization can extend context limits, but uncached prefill can still leave long-context SLO goodput far below the short-context baseline.

D. Hardware assignments are not stable

Can a fleet commit each serving role to one accelerator class? Changing the objective from goodput per kW to goodput per deployment unit moves six of eight best deployments from systolic to GPU-based hardware. We measure lock-in by varying specification corner, context, model direction, or objective, changing only each nominal-best 128 kW deployment's batch. With comparisons and axes weighted equally, the median loss is 35.7% of scenario-best SLO goodput per kW (per unit on the objective axis). Re-optimizing mappings and pool sizes within the existing hardware cuts this loss to 9.3%. Beyond remapping, a 25% reserve of units or power lowers it to 5.1%, and switching the serving design lowers it to 5.7%. Doubling inter-pool bandwidth lowers it only to 9.2%. None of these changes supplies an absent accelerator class.

Takeaway 4. The evidence supports capability preservation rather than early lock-in. Fleet planners should let the serving decomposition and hardware assignment follow the models they serve. They should keep mappings and pool sizes adjustable rather than lock a future fleet to the accelerator class with the highest score at one operating point.

V. Calibration and Robustness Testing

A. Governing equations

Each role's service time follows its busiest chip's compute and memory work. Role $r \in \{\mathrm{A}, \mathrm{F}\}$ has per-microbatch layer time $t_r = \max(\Phi_r, \Theta_r) + (1-\gamma)\min(\Phi_r, \Theta_r) + t_{\mathrm{TP}} + t_0$ in Eq. (1). Here Φ_r and Θ_r are compute and memory times, γ their calibrated overlap ratio, t_{TP} TP all-reduce time, and t_0 fixed per-layer launch latency. Each microbatch re-streams its weights and pays t_0.

Exchange. Both designs pay for expert dispatch and combine across scale-up and scale-out tiers. Dispatch sends each token of width d to $k_e = k + n_{\mathrm{sh}}$ experts (shared ones always active) at σ_{D} bytes per element. t_{D} adds per-hop latency for every touched scale-up domain to the slower of injection, $b_s k_e d\sigma_{\mathrm{D}}/\beta_{\mathrm{inj}}$, and ejection, $\iota\, b k_e d\sigma_{\mathrm{D}}/(\mathrm{EP}\,\beta_{\mathrm{ej}})$. Here b_s is the sending rank's token count, β_{inj} and β_{ej} are endpoint bandwidths, and $\iota = 1$ gives mean receiver load. Combine uses the same rule with $\sigma_{\mathrm{C}} = 2\sigma_{\mathrm{D}}$ (FP8 dispatch, 16-bit combine). The model includes endpoint bandwidth limits without tracing switch paths or simulating network queues. Experts are spread evenly over EP ranks, fractionally when EP does not divide the expert count.

Capacity. Memory available for KV state bounds concurrency. A unit of capacity H has $\phi H - H_c$ usable memory, with $\phi = 0.9$ [144] and communication buffer $H_c = 2\,\mathrm{GiB}$; SRAM/dataflow uses its full SRAM. Resident requests U are capped at $\mathrm{DP_A}\, s_{\mathrm{kv}}(\phi H - H_c - \omega)/((C+O)\kappa)$. $\mathrm{DP_A}$ counts attention replicas, s_{kv} is the KV shard factor, κ KV bytes per token, $C+O$ the peak resident context after O output tokens, and ω other resident state.

Waiting and SLO goodput. We convert service times into SLO goodput with a queue per pool. For Poisson arrivals at rate λ and c servers of rate μ, Erlang-C gives queueing probability $P_Q(c, \lambda/(c\mu))$ [52]. Conditional wait is exponential with Allen–Cunneen rate $2(c\mu-\lambda)/(1+v^2)$ [7], where v^2 is the service-time squared coefficient of variation. Nominal $v^2 = 1$ is conservative for the fixed-length workload. Decode's U slots of rate $1/(OT)$ saturate at X/O requests/s. Prefill has R_{P} replicas of b_{P} slots at rate $1/t_{\mathrm{P}}$. Given $T \le S_{\mathrm{TPOT}}$ and $\lambda < c\mu$ in each pool, SLO goodput is the largest λ satisfying $t_{\mathrm{P}} + t_{\mathrm{KV}} + T/M + W_{99} \le S_{\mathrm{TTFT}}$. t_{KV} is the KV handoff, W_{99} the exact p99 of the summed prefill and decode waits $W_{\mathrm{P}} + W_{\mathrm{D}}$, and T/M bounds the microbatch-boundary wait.

Queue scope. The fixed-order schedule folds per-layer synchronization and attention–FFN backpressure into T. The queue omits batch coupling, stragglers, and decode-to-prefill backpressure, and treats the two waits as independent.

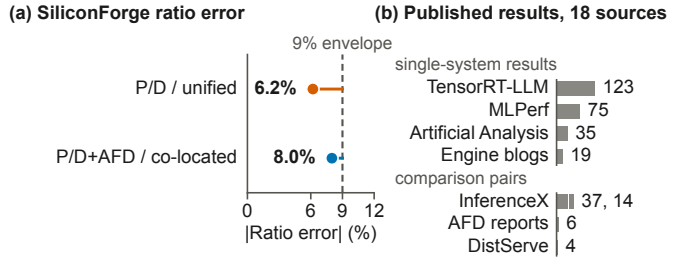


Fig. 11. **Comparative errors against the 9% envelope.** (a) Ratio errors (dots) and distance to the 9% envelope (segments; §V-C). (b) Published prediction checks by source.

B. Frozen calibration and validation

We freeze four timing effects across all evaluation scenarios: GEMV-to-GEMM bandwidth Hill curves (per class where public data support them), a common sustained-to-peak compute ratio η, per-layer launch latency t_0, and compute/memory overlap γ. Calibration used published low-concurrency token rates without target-specific tuning. We compare the frozen model's throughput and between-design ratios [53] with 252 throughput results and 47 primary comparison pairs from 18 published sources (Figure 11b). The AFD and InferenceX [125] pairs were held out from tuning under a preregistered protocol fixing the model and drivers before prediction. Figure 11a compares errors with the 9% envelope (§V-C).

The AFD checks use fixed configurations at saturated decode throughput without an SLO [2], [43], sometimes with forced expert balancing and logical-scale emulation. The primary check of unified and P/D frontiers at matched per-user rates [125] fails because under-predicted TTFT admits configurations excluded by the measured frontier. A later DistServe driver under-predicts P/D's advantage [161]. Some published speedups were known before prediction. Absolute single-system throughput is substantially over-predicted [12], [79], [82]–[85], [101], [107]–[109], [136]–[138], [155].

AFD checks cover fixed configurations within one scale-up domain; no published pair spans two studied accelerator classes. Other reports lack per-design steady-state goodput [11], [145] or the realized mapping [142], [148] and cannot be matched. Testing complete-deployment model estimates needs both designs' measured p99 TTFT, TPOT, steady-state goodput, and realized mapping near saturation on the same model, hardware, engine, and budget. An event-driven simulation checks only the queueing closed forms (§V-A). Goodput margins agree within 0.2 percentage points; closed forms conservatively estimate p99 TTFT near saturation.

C. When a modeled difference is interpretable

For headline comparisons, the *margin* Δ in SLO goodput per kW is (P/D+AFD − P/D)/P/D; positive values favor P/D+AFD. The two-part test calls a comparison *decided*, with a *robust* margin, when the same design leads at every tested specification corner and nominal $|\Delta|$ exceeds the *9% envelope*; otherwise, it is *undecided*. Corners represent specification uncertainty, not a sampling distribution, and do not establish behavior between them. Published inference-error summaries

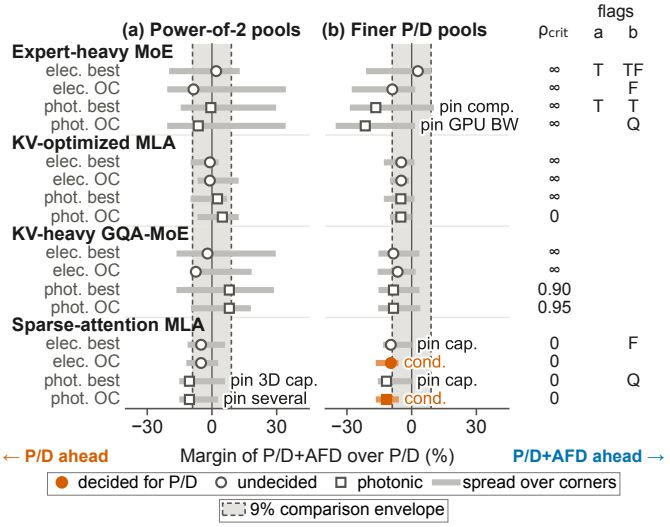


Fig. 12. **Headline verdicts under both pool-sizing rules.** best: best-allowed; OC: one-class; cond.: conditional; pin: range deciding the row when pinned (BW: memory bandwidth; several: no single range); ρ_{crit} (Figure 12a): least sign-preserving error correlation (∞: none). Pre-declared Figure 12a–b flags: T, within 10% of the TPOT target; Q, verdict changes with $v^2{=}4$ or saturation throughput instead of SLO goodput; F, verdict changes with another collective or link convention.

anchor the 9% comparison envelope [3], [40], [158]. Verdicts passing 9% but not the largest observed AFD gain error are *conditional*, as are all role-specific verdicts because no published pair spans two studied classes.

D. Applying the two-part test

We independently re-optimize both designs at each tested specification corner. Figure 12 shows nominal margins (markers) and corner ranges (bars) against the 9% envelope. Under the main rule (Figure 12a), every range spans both signs; no headline comparison is decided. With finer P/D pools (Figure 12b), one-class sparse attention conditionally favors P/D beyond 9% on both fabrics. No P/D+AFD or best-allowed comparison is decided. Best-allowed sparse attention ties at one corner where the same prefill pool limits both designs.

Error cancellation. We sweep error correlation in Monte Carlo with 9% error per candidate deployment, re-selecting each design's best without extrapolating the six AFD pairs' measured cancellation. Figure 12's ρ_{crit} is the least correlation preserving the nominal lead in 95% of draws (∞: none).

Robustness. Under the main rule, halved t_0, $\gamma = 0.5$ or 1.0, v^2 up to 4, collective or link conventions, pipeline fill and drain, a straggler, capacity–bandwidth coupling, and $M \leq 2$ leave headline comparisons undecided but can move nominal margins. Less usable memory ($\phi = 0.8$) can favor P/D+AFD, while prefix reuse can favor either design. Halved ranges decide photonic sparse attention for P/D. With finer P/D pools, speculative decoding (§VI) or full usable memory ($\phi = 1$) can undo one-class preferences; all added verdicts favor P/D.

Whole-expert EP divisors give no nominal P/D+AFD lead beyond 9%. Their main-rule subset caps KV-heavy's P/D pool at 64 units and can create such a lead.

VI. Discussion and Scope

Serving and capacity model. Both designs use the same queueing and capacity model. Design-specific scheduler or prefix-reuse policies do not enter the margin. Other policies, parallelism, or distributed prefill may change feasibility.

Large expert parallelism can narrow what AFD adds. Published decode deployments use EP 72–320 [32], [33], [138], [163]. Large EP gives co-located decode the FFN batching of AFD's second pool. At 512 kW, forcing both designs to EP 64 or 128 can flip GPU one-class margins toward P/D. With EP re-optimized, electrical best-allowed margins remain within the 9% envelope. We omit EP beyond the expert count and configurations with redundant experts.

Expert imbalance is an evaluated sensitivity. SiliconForge can estimate the busiest EP rank's load under uniform random routing with a binomial model, charging it to routed FFN work and receiving traffic. We evaluated this sensitivity with dedicated links at 32K context, at 128 kW for one-class and best-allowed placement and at 512 kW for GPU one-class placement. With EP re-optimized, no margin changes sign or its side of the 9% envelope.

New fabric features are link parameters. NVLink 5 and 6, SHARP, NVLink Fusion, and device-initiated RDMA [13], [51], [99], [102] map to tier bandwidth, latency, domain size, and collective offload. SHARP speeds all-reduce, not dispatch and combine. In headline comparisons, no tested named link gives P/D+AFD a lead beyond 9% under either pool-sizing rule. Small domains give AFD a nominal lead (§IV-B).

Extending to speculative and diffusion decoding. Speculative decoding can place a small draft and larger verifier in separate pools [19] and increases both designs' FFN tokens per weight read [32], [65], [66]. In our one-draft-token sensitivity, which omits draft cost and draft or transient KV state, KV-optimized MLA's one-class AFD lead in throughput per decode kW begins at nearly twice the context. Full-serving SLO goodput includes prefill under the common budget; this sensitivity establishes no P/D+AFD preference under either pool-sizing rule (§V-C). Unevaluated diffusion decoding raises tokens per weight read [54], [91] and repeats prefill [37], [59].

VII. Related Work

Serving disaggregation. DistServe and Splitwise separate prefill from decode [113], [161]; Mooncake emphasizes KV transfer and reuse [117], and P/D-Serve and HexGen-2 demonstrate large-scale and heterogeneous deployments [57], [58]. Dynamo, SGLang, llm-d, and Corsair provide production P/D paths [30], [74], [97], [126]. Heterogeneous-P/D studies show accelerator class, precision, fabric, and KV residency change the hardware assignment [146], [147]. These systems fix the boundary at P/D. Splitwise asks which silicon should serve each phase. We ask this at the attention/FFN boundary.

MegaScale-Infer, Step-3, xDeepServe, Janus, Lamina, AiDE, and Rubin–LPX use an attention/FFN split [14], [24], [60], [132], [152], [160], [162]. Measurements, models, and sweeps show that AFD's value depends on the model, workload, and fabric [67], [72], [81], [131], [150]. AFD's measured gain changes sign with pool provisioning [2]. A gain at one deployment does not settle the boundary choice before future model demands and hardware resources are known.

Closest design-space models. Wu et al. search parallelism, P/D, and AFD on 128 B200 GPUs, deferring unreleased hardware [150]; we re-evaluate one case in §IV-C. Song et al. study A/F provisioning under stochastic workload variation using latency models calibrated on Huawei Ascend 910C NPUs [131]. Their closed-form rule assumes a compute-bound FFN, with no co-located baseline. Their FFN arithmetic intensity is 299 FLOP per weight byte. This lies below the FP8 ridge of B200 and our GPU and systolic classes, where the attention-to-FFN ratio scales with FFN memory bandwidth. Frontier's simulations flip the P/D-versus-AFD ranking with the TTFT SLO [40]. Liu et al. trace an AFD "dead zone" to scale-out bandwidth [72]. These four studies evaluate fixed hardware. Models and simulators cover current and prospective systems [3], [17], [18], [22], [26], [53], [149], [153], [158]. Statistical methods track model error and quantify predictive confidence over measured systems [6], [16], [25], [50], [92], [122], [151], [154]. Prospective SPAD, Rubin CPX, memory-centric attention, and Raptor studies illustrate the need to combine these practices for hardware that cannot yet be run [89], [100], [111], [156], [159]. We vary future LLM architecture directions anchored in published families and hardware resource ranges anchored in announced accelerators (Tables III and II). Regime and pool-sizing searches recorded about 59.5 million decode candidate evaluations; both designs are re-optimized under a common budget at each specification corner. We compare nominal margins with model error and test whether their signs survive specification uncertainty.

Concurrent work. Three studies posted after the initial submission report related conditions. OpWeave proves that one-class operator splitting pays only once KV growth pushes the co-located batch below the compute-bound threshold [68]. HeteroPanacea finds that adding AFD to P/D pays only on genuinely different devices [41]. Under a common budget, AFD-Ledger selects one-class AFD in 7 of 36 settings [118]. SQD instead splits decode at the quadratic/subquadratic attention boundary [140]. Our comparison tests P/D against P/D+AFD across future LLM architecture directions and jointly varied hardware-specification ranges.

VIII. Conclusion

SiliconForge separates serving decomposition from hardware assignment. Headline comparisons lean P/D without a robust AFD advantage. AFD nominally leads for the KV-heavy direction when the co-located expert pool spans small scale-up domains. Hardware assignments change with objectives and specification corners. Prospective modeling informs substantial fleet investments that shape customer experience and accelerator roadmaps. We recommend keeping mappings and pool sizes adjustable.

REFERENCES

[1] D. Abts, G. Kimmell, A. C. Ling, J. Kim, M. Boyd, A. Bitar, S. Parmar, I. Ahmed, R. DiCecco, D. Han, J. Thompson, M. Bye, J. Hwang, J. Fowers, P. Lillian, A. Murthy, E. Mehtabuddin, C. Tekur, T. Sohmers, K. Kang, S. Maresh, and J. Ross, "A software-defined tensor streaming multiprocessor for large-scale machine learning," in *Proceedings of the 49th Annual International Symposium on Computer Architecture (ISCA)*, 2022, pp. 567–580.

[2] AFD Plugin Contributors, "Announcing vLLM AFD plugin: Disaggregating attention and FFN for flexible MoE serving," vLLM Blog, https://vllm.ai/blog/2026-07-23-vllm-afd-plugin, Jul. 2026, published 2026-07-23; accessed 2026-09-28.

[3] A. Agrawal, N. Kedia, J. Mohan, A. Panwar, N. Kwatra, B. S. Gulavani, R. Ramjee, and A. Tumanov, "Vidur: A large-scale simulation framework for LLM inference," in *Proceedings of Machine Learning and Systems (MLSys)*, 2024.

[4] A. Agrawal, N. Kedia, A. Panwar, J. Mohan, N. Kwatra, B. S. Gulavani, A. Tumanov, and R. Ramjee, "Taming throughput-latency tradeoff in LLM inference with Sarathi-Serve," in *Proceedings of the 18th USENIX Symposium on Operating Systems Design and Implementation (OSDI)*, 2024, pp. 117–134.

[5] J. Ainslie, J. Lee-Thorp, M. de Jong, Y. Zemlyanskiy, F. Lebrón, and S. Sanghai, "GQA: Training generalized multi-query transformer models from multi-head checkpoints," in *Proceedings of the 2023 Conference on Empirical Methods in Natural Language Processing (EMNLP)*, 2023, pp. 4895–4901.

[6] A. R. Alameldeen and D. A. Wood, "Variability in architectural simulations of multi-threaded workloads," in *Proceedings of the 9th International Symposium on High-Performance Computer Architecture (HPCA)*, 2003, pp. 7–18.

[7] A. O. Allen, *Probability, Statistics, and Queueing Theory with Computer Science Applications*, 2nd ed. Boston, MA: Academic Press, 1990.

[8] Amazon Web Services, "Amazon EC2 Inf2 instances," Product page, https://aws.amazon.com/ec2/instance-types/inf2/, 2023, Inferentia2 instance and accelerator specifications. Accessed 2026-07-30.

[9] Amazon Web Services, "Amazon EC2 Trn2 instances," Product page, https://aws.amazon.com/ec2/instance-types/trn2/, 2024, Trainium2 instance and accelerator specifications. Accessed 2026-07-30.

[10] AMD, "Accelerator specifications," Product specification catalog, https://www.amd.com/en/products/specifications/accelerators.html, 2026, catalog source for the MI300X, MI325X, and MI355X entries. Accessed 2026-07-30.

[11] AMD and Embedded LLM, "Next-level inference: Why your single-node vLLM setup needs prefill-decode disaggregation," vLLM Blog, https://vllm.ai/blog/2026-04-07-moriio-kv-connector, Apr. 2026, accessed 2026-10-05.

[12] Artificial Analysis, "Independent performance analysis of leading GPUs: AMD MI300X, NVIDIA H100, NVIDIA H200," https://artificialanalysis.ai/articles/independent-analysis-of-leading-gpus-amd-nvidia, Jun. 2025, dated 2025-06-08; System Load Test; values digitized from the published charts. Accessed 2026-09-28.

[13] K. Aubrey, "Inside the NVIDIA Vera Rubin platform: Six new chips, one AI supercomputer," NVIDIA Technical Blog, https://developer.nvidia.com/blog/inside-the-nvidia-rubin-platform-six-new-chips-one-ai-supercomputer/, Jan. 2026, published 2026-01-05; accessed 2026-09-28.

[14] K. Aubrey and F. Ghodsian, "Inside NVIDIA Groq 3 LPX: The low-latency inference accelerator for the NVIDIA Vera Rubin platform," NVIDIA Technical Blog, https://developer.nvidia.com/blog/inside-nvidia-groq-3-lpx-the-low-latency-inference-accelerator-for-the-nvidia-vera-rubin-platform/, Mar. 2026, published 2026-03-16; accessed 2026-09-28. Table 2: per 8-LPU tray 9.6 PFLOPS FP8, 4 GB SRAM at 1.2 PB/s, up to 256 + 128 GB DRAM, 20 TB/s scale-up.

[15] Ayar Labs, "TeraPHY optical I/O chiplet," https://ayarlabs.com/teraphy/, 2025, 8 Tbps bidirectional; 8 full-duplex optical ports at 512 Gbps per port per direction; 16 WDM transceiver slices per port; UCIe-compliant. Accessed 2026-07-31.

[16] D. Balamurugan and T. W. Bush, "OmniPilot: An uncertainty-aware LLM inference advisor for heterogeneous GPU clusters," arXiv preprint arXiv:2607.01579, 2026.

[17] A. Bambhaniya, R. Raj, G. Jeong, S. Kundu, S. Srinivasan, S. Subramanian, M. Elavazhagan, M. Kumar, and T. Krishna, "Demystifying AI platform design for distributed inference of next-generation LLM models," arXiv preprint arXiv:2406.01698, 2024, v3, May 2025; tool released as GenZ-LLM-Analyzer.

[18] A. R. Bambhaniya, H. Wu, S. Subramanian, S. Srinivasan, S. Kundu, A. Yazdanbakhsh, M. Elavazhagan, M. Kumar, M. Yu, A. Raychowdhury, and T. Krishna, "MIST: A co-design framework for heterogeneous, multi-stage LLM inference," arXiv preprint arXiv:2504.09775, 2025.

[19] J. Bartlett, N. Serrino, Z. Asgar, S. Bhoja, P. Nair, N. Ghanathe, and N. Kurella, "Low-latency inference with speculative decoding on d-Matrix Corsair and GPU," Gimlet Labs Blog, https://gimletlabs.ai/blog/low-latency-spec-decode-corsair, Mar. 2026, mixed measured and modeled study. Accessed 2026-07-30.

[20] Cerebras Systems, "Cerebras Systems unveils world's fastest AI chip with whopping 4 trillion transistors," https://www.cerebras.ai/press-release/cerebras-announces-third-generation-wafer-scale-engine, 2024, WSE-3: 4T transistors, 900,000 AI cores, 44 GB on-chip SRAM, 21 PB/s on-chip bandwidth, 125 PFLOPS peak, TSMC 5nm.

[21] C. Chen, "Transformer inference arithmetic," https://kipp.ly/transformer-inference-arithmetic/, 2022, accessed 2026-07-16.

[22] H. Chen, X. Liu, Y. Liu, J. Jiang, B. He, and X. Liu, "FleetOpt: Analytical fleet provisioning for LLM inference with compress-and-route as implementation mechanism," arXiv preprint arXiv:2603.16514, 2026, work in progress.

[23] J. Chen, Y. Zhuang, and H. Zhang, "Disaggregated inference: 18 months later," Hao AI Lab Blog, https://haoailab.com/blogs/distserve-retro/, Nov. 2025, published 2025-11-03; accessed 2026-09-28.

[24] S. Chen, W. Xiao, Y. Lin, M. Zhang, Y. Shan, J. Jiang, K. Chen, and Y. Wu, "Efficient heterogeneous large language model decoding with model-attention disaggregation," arXiv preprint arXiv:2405.01814, 2024, version 2, revised 2025-04-10.

[25] T. Chen, Y. Chen, Q. Guo, O. Temam, Y. Wu, and W. Hu, "Statistical performance comparisons of computers," in *Proceedings of the 18th IEEE International Symposium on High-Performance Computer Architecture (HPCA)*, 2012, pp. 399–410.

[26] J. Cho, H. Choi, G. Heo, and J. Park, "LLMServingSim 2.0: A unified simulator for heterogeneous and disaggregated LLM serving infrastructure," in *Proceedings of the IEEE International Symposium on Performance Analysis of Systems and Software (ISPASS)*, 2026, pp. 1–14.

[27] J. Choquette, "NVIDIA Hopper H100 GPU: Scaling performance," *IEEE Micro*, vol. 43, no. 3, pp. 9–17, 2023.

[28] A. Clark, D. de Las Casas, A. Guy, A. Mensch, M. Paganini, J. Hoffmann, B. Damoc, B. Hechtman, T. Cai, S. Borgeaud, G. B. van den Driessche, E. Rutherford, T. Hennigan, M. J. Johnson, A. Cassirer, C. Jones, E. Buchatskaya, D. Budden, L. Sifre, S. Osindero, O. Vinyals, M. Ranzato, J. Rae, E. Elsen, K. Kavukcuoglu, and K. Simonyan, "Unified scaling laws for routed language models," in *Proceedings of the 39th International Conference on Machine Learning (ICML)*, 2022, pp. 4057–4086.

[29] d-Matrix, "d-Matrix and Alchip announce collaboration on world's first 3D DRAM solution to supercharge AI inference," https://www.d-matrix.ai/announcements/d-matrix-and-alchip-announce-collaboration-on-worlds-first-3d-dram-solution-to-supercharge-ai-inference/, 2025, press announcement.

[30] d-Matrix, "d-Matrix Corsair AI inference platform enters full production to meet customer demand," https://www.d-matrix.ai/announcements/d-matrix-corsair-ai-inference-platform-enters-full-production-to-meet-customer-demand/, Jun. 2026, Corsair serves decode paired with GPU prefill. Accessed 2026-07-29.

[31] DeepSeek-AI, "DeepSeek-V2: A strong, economical, and efficient mixture-of-experts language model," arXiv preprint arXiv:2405.04434, 2024.

[32] DeepSeek-AI, "DeepSeek-V3 technical report," arXiv preprint arXiv:2412.19437, 2024.

[33] DeepSeek-AI, "Day 6: One more thing, DeepSeek-V3/R1 inference system overview," DeepSeek Open Infra Index, https://github.com/deepseek-ai/open-infra-index/blob/main/202502OpenSourceWeek/day_6_one_more_thing_deepseekV3R1_inference_system_overview.md, Feb. 2025, published 2025-02-28 (Open Source Week); accessed 2026-09-28.

[34] DeepSeek-AI, "DeepSeek-V3.2: Pushing the frontier of open large language models," arXiv preprint arXiv:2512.02556, 2025.

[35] DeepSeek-AI, "DeepSeek-V4: Towards highly efficient million-token context intelligence," arXiv preprint arXiv:2606.19348, 2026.

[36] A. Elmeleegy, "How NVIDIA Dynamo 1.0 powers multi-node inference at production scale," NVIDIA Technical Blog, https://developer.nvidia.com/blog/nvidia-dynamo-1-production-ready/, Mar. 2026, published 2026-03-16; accessed 2026-09-28.

[37] J. Fan, Y. Zhang, X. Li, and D. S. Nikolopoulos, "Taming the memory footprint crisis: System design for production diffusion LLM serving," arXiv preprint arXiv:2512.17077, 2025, version 2, 2026-01-14.

[38] X. Fan, W.-D. Weber, and L. A. Barroso, "Power provisioning for a warehouse-sized computer," in *Proceedings of the 34th Annual International Symposium on Computer Architecture (ISCA)*, 2007, pp. 13–23.

[39] W. Fedus, B. Zoph, and N. Shazeer, "Switch transformers: Scaling to trillion parameter models with simple and efficient sparsity," *Journal of Machine Learning Research*, vol. 23, no. 120, pp. 1–39, 2022.

[40] Y. Feng, X. Tan, Y. Deng, Y. Jiang, Y. Zhu, and H. Xu, "Frontier: Towards comprehensive and accurate LLM inference simulation," arXiv preprint arXiv:2605.21312, 2026, version 2, revised 2026-06-13.

[41] P. Forys, H. Wu, C. Xiao, J. Nie, T. Liu, R. Antonova, T. Jones, R. Mullins, W. Luk, A. Zhao, and G. A. Constantinides, "When does disaggregation pay? Simulating prefill–decode–attention–FFN specialization for agentic LLM inference," arXiv preprint arXiv:2608.03741, 2026, version 1, 2026-08-04.

[42] Fractile, "Radically accelerate frontier model inference," https://www.fractile.ai/, 2026, in-memory-compute inference accelerator; presilicon, with commercial hardware availability reported for 2027. Accessed 2026-07-29.

[43] Y. Fu, Y. Zhang, R. Wang, J. Chen, and H. Zhang, "FastAFD: Open-source large-scale attention–FFN disaggregation on Blackwell NVL72," Hao AI Lab technical blog and open-source release, https://haoailab.com/blogs/fastafd/, Jul. 2026, published 2026-07-06; code at https://github.com/hao-ai-lab/FastAFD (commit 3c71619); accessed 2026-09-28.

[44] FuriosaAI, "RNGD specifications," Product specification page, https://furiosa.ai/renegade-spec, 2024, accelerator compute, memory, interface, and power specifications. Accessed 2026-07-30.

[45] Google Cloud, "TPU v5e," Cloud TPU documentation, https://docs.cloud.google.com/tpu/docs/v5e, 2023, architecture and per-chip specifications. Accessed 2026-07-30.

[46] Google Cloud, "TPU v5p," Cloud TPU documentation, https://docs.cloud.google.com/tpu/docs/v5p, 2023, architecture and per-chip specifications. Accessed 2026-07-30.

[47] Google Cloud, "TPU v6e (Trillium)," https://docs.cloud.google.com/tpu/docs/v6e, 2024, GA 2024-12-16, accessed 2026-07-15. Per chip: 918 TFLOPS BF16, 1836 TOPS INT8, 32 GB HBM, 1638 GB/s HBM bandwidth, 800 GB/s bidirectional ICI; 256-chip pod, 2D torus.

[48] Google Cloud, "TPU7x (Ironwood)," https://docs.cloud.google.com/tpu/docs/tpu7x, 2026, announced Google Cloud Next 2025; preview 2025-11-24; GA 2026-03-31; docs accessed 2026-09-28. Per chip: 4614 TFLOPS FP8, 2307 TFLOPS BF16, 192 GiB HBM, 7380 GB/s HBM bandwidth, 1200 GB/s bidirectional ICI, 100 Gb/s DCN; 9,216-chip pod.

[49] D. Guo, D. Yang, H. Zhang *et al.*, "DeepSeek-R1 incentivizes reasoning in LLMs through reinforcement learning," *Nature*, vol. 645, no. 8081, pp. 633–638, 2025.

[50] A. Gutierrez, J. Pusdesris, R. G. Dreslinski, T. N. Mudge, C. Sudanthi, C. D. Emmons, M. Hayenga, and N. C. Paver, "Sources of error in full-system simulation," in *Proceedings of the IEEE International Symposium on Performance Analysis of Systems and Software (ISPASS)*, 2014, pp. 13–22.

[51] K. Hamidouche, J. Bachan, P. Markthub, P.-J. Gootzen, E. Agostini, S. Jeaugey, A. Shafi, G. Theodorakis, and M. G. Venkata, "GPU-initiated networking for NCCL," arXiv preprint arXiv:2511.15076, 2025, version 2, 2025-11-24.

[52] M. Harchol-Balter, *Performance Modeling and Design of Computer Systems: Queueing Theory in Action*. Cambridge, UK: Cambridge University Press, 2013.

[53] M. D. Hill and V. J. Reddi, "Gables: A roofline model for mobile SoCs," in *Proceedings of the 25th IEEE International Symposium on High-Performance Computer Architecture (HPCA)*, 2019, pp. 317–330.

[54] Inception Labs, S. Khanna, S. Kharbanda, S. Li, H. Varma, E. Wang, S. Birnbaum, Z. Luo, Y. Miraoui, A. Palrecha, S. Ermon, A. Grover, and V. Kuleshov, "Mercury: Ultra-fast language models based on diffusion," arXiv preprint arXiv:2506.17298, 2025, version 1, 2025-06-17.

[55] Intel, "Intel Gaudi 3 AI Accelerator HL-338 PCIe Card Product Brief," Product brief, https://cdrdv2-public.intel.com/817488/Gaudi%203%20PCIe%20Product%20Brief_RB_1_V6.pdf, 2025, HL-338 PCIe accelerator specifications. February 2025 revision, document 360231-002US. Accessed 2026-10-09.

[56] A. Q. Jiang, A. Sablayrolles, A. Roux, A. Mensch, B. Savary, C. Bamford, D. S. Chaplot, D. de las Casas, E. B. Hanna, F. Bressand, G. Lengyel, G. Bour, G. Lample, L. R. Lavaud, L. Saulnier, M.-A. Lachaux, P. Stock, S. Subramanian, S. Yang, S. Antoniak, T. L. Scao, T. Gervet, T. Lavril, T. Wang, T. Lacroix, and W. E. Sayed, "Mixtral of experts," arXiv preprint arXiv:2401.04088, 2024.

[57] Y. Jiang, R. Yan, and B. Yuan, "HexGen-2: Disaggregated generative inference of LLMs in heterogeneous environment," in *Proceedings of the 13th International Conference on Learning Representations (ICLR)*, 2025.

[58] Y. Jin, T. Wang, H. Lin, M. Song, P. Li, Y. Ma, Y. Shan, Z. Yuan, C. Li, Y. Sun, T. Wu, X. Chu, R. Huan, L. Ma, X. You, W. Zhou, Y. Ye, W. Liu, X. Xu, Y. Zhang, T. Dong, J. Zhu, Z. Wang, X. Ju, J. Song, H. Cheng, X. Li, J. Ding, H. Guo, and Z. Zhang, "P/D-Serve: Serving disaggregated large language model at scale," arXiv preprint arXiv:2408.08147, 2024.

[59] N. Kedia, S. Agarwal, M. Lee, and A. Akella, "Sangam: Efficiently serving diffusion LLMs with the AR stack," arXiv preprint arXiv:2607.04206, 2026, version 1, 2026-07-05.

[60] K. Kim, O. Kwon, Y. Park, and J. W. Lee, "AiDE: Attention-FFN disaggregated execution for cost-effective LLM decoding on CXL-PNM," *IEEE Computer Architecture Letters*, vol. 24, no. 2, pp. 285–288, 2025.

[61] Kimi Team, "Kimi K2: Open agentic intelligence," arXiv preprint arXiv:2507.20534, 2025.

[62] W. Kwon, Z. Li, S. Zhuang, Y. Sheng, L. Zheng, C. H. Yu, J. E. Gonzalez, H. Zhang, and I. Stoica, "Efficient memory management for large language model serving with PagedAttention," in *Proceedings of the 29th Symposium on Operating Systems Principles (SOSP)*, 2023, pp. 611–626.

[63] X. Lai, W. Xu, Y. Yang, Q. Chen, Y. Xu, L. Zeng, X. Li, H. Sun, H. Zhu, V. Zhang, J. Hu, J. Li, R. Gao, Z. Li, S. Zhu, J. Zhou, and P. Zhao, "MiniMax sparse attention," arXiv preprint arXiv:2606.13392, 2026, the MiniMax-M3 technical report.

[64] D. Lepikhin, H. Lee, Y. Xu, D. Chen, O. Firat, Y. Huang, M. Krikun, N. Shazeer, and Z. Chen, "GShard: Scaling giant models with conditional computation and automatic sharding," in *Proceedings of the 9th International Conference on Learning Representations (ICLR)*, 2021.

[65] Y. Leviathan, M. Kalman, and Y. Matias, "Fast inference from transformers via speculative decoding," in *Proceedings of the 40th International Conference on Machine Learning (ICML)*, 2023, pp. 19 274–19 286.

[66] Y. Li, F. Wei, C. Zhang, and H. Zhang, "EAGLE: Speculative sampling requires rethinking feature uncertainty," in *Proceedings of the 41st International Conference on Machine Learning (ICML)*, ser. Proceedings of Machine Learning Research, vol. 235, 2024, pp. 28 935–28 948.

[67] Z. Li, "Operator-level disaggregated serving for efficient LLM inference," Carnegie Mellon University CSD PhD Blog, https://www.cs.cmu.edu/~csd-phd-blog/2026/operator-level-disaggregated-serving/, May 2026, accessed 2026-07-16.

[68] Z. Li, Y. Mei, S. Pan, Z. Chen, X. Zhang, M. Wu, S. Lin, Y. Yang, Z. Zhang, X. Miao, R. Vinayak, and Z. Jia, "OpWeave: Flexible operator disaggregation for heterogeneous LLM serving," arXiv preprint arXiv:2609.14237, 2026, version 1, 2026-09-13.

[69] Lightmatter, "Lightmatter announces Passage L200, the fastest co-packaged optics for AI," Press release, https://lightmatter.co/press-release/lightmatter-announces-passage-l200-the-fastest-co-packaged-optics-for-ai/, Mar. 2025, 2025-03-31. L200 32 Tbps and L200X 64 Tbps (Tx+Rx); over 200 Tbps per package; available 2026. Accessed 2026-09-28.

[70] Lightmatter, "Passage M1000: A 3D photonic interposer for AI," 2025 IEEE Hot Chips 37 Symposium (HCS), https://hc2025.hotchips.org/assets/program/conference/day2/57-lightmatter_hotchips_2025_final.pdf, 2025, 114 Tbps total optical bandwidth (57 Tbps each direction); $>$4,000 mm^2 multi-reticle active photonic interposer; 1024 electrical SerDes at 56 Gbps; 256 fibers at 448 Gbps each; built-in solid-state optical circuit switching.

[71] Lightmatter, "Passage: 3D photonics for AI," Product overview, https://lightmatter.co/products/passage-v2/, 2026, single-chip through multi-die and wafer-scale photonic interconnect roadmap; accessed 2026-07-30; archived 2026-04-14 state: http://web.archive.org/web/20260414144320/https://lightmatter.co/products/passage-v2/.

[72] G. Liu, H. Li, Y. Guo, Y. Lyu, M. Zhou, Y. Liu, Z. Li, and Y. Wang, "Revealing the challenges of attention-FFN disaggregation for modern MoE models and hardware systems," arXiv preprint arXiv:2602.09721, 2026.

[73] Llama Team, AI @ Meta, "The Llama 3 herd of models," arXiv preprint arXiv:2407.21783, 2024.

[74] llm-d Community, "llm-d: Kubernetes-native distributed inference serving," https://llm-d.ai/, 2025, software; accepted as a CNCF Sandbox project on 2026-03-12 (announced 2026-03-24). Accessed 2026-07-16.

[75] E. Lu, Z. Jiang, J. Liu, Y. Du, T. Jiang, C. Hong, S. Liu, W. He, E. Yuan, Y. Wang, Z. Huang, H. Yuan, S. Xu, X. Xu, G. Lai, Y. Chen, H. Zheng, J. Yan, J. Su, Y. Wu, Y. Zhang, Z. Yang, X. Zhou, M. Zhang, and J. Qiu, "MoBA: Mixture of block attention for long-context LLMs," in *Advances in Neural Information Processing Systems 38 (NeurIPS)*, 2025, arXiv:2502.13189.

[76] MatX, "MatX One," https://matx.com/, 2026, transformer-focused inference accelerator: weights in SRAM, KV cache in HBM. No public datasheet. Accessed 2026-07-29.

[77] Meta, "How Meta is creating custom silicon for AI," Engineering at Meta, https://engineering.fb.com/2023/10/18/ml-applications/meta-ai-custom-silicon-olivia-wu/, 2023, first-generation MTIA provenance. Accessed 2026-07-30.

[78] Meta, "Introducing the next-gen Meta Training and Inference Accelerator," Engineering at Meta, https://engineering.fb.com/2024/04/10/ml-applications/next-gen-mtia-meta-training-inference-accelerator/, 2024, second-generation MTIA provenance and specifications. Accessed 2026-07-30.

[79] Meta and NVIDIA Team, "Driving vLLM WideEP and large-scale serving toward maturity on Blackwell (Part I)," vLLM Blog, https://vllm.ai/blog/2026-02-03-dsr1-gb200-part1, Feb. 2026, accessed 2026-09-28.

[80] Microsoft, "Inside Maia 100: Revolutionizing AI workloads with Microsoft's custom AI accelerator," Microsoft Azure Infrastructure Blog, https://techcommunity.microsoft.com/blog/azureinfrastructureblog/inside-maia-100-revolutionizing-ai-workloads-with-microsofts-custom-ai-accelerat/4229118, 2024, Hot Chips 2024 architecture and system specifications. Accessed 2026-07-30.

[81] T. Mitra, R. Borkar, N. Bhatia, R. Matas, S. Raj, D. Mudigere, R. Zhao, M. Golub, A. Dutta, S. Madduri, D. Jani, B. Pharris, and B. D. Rouhani, "Beyond the buzz: A pragmatic take on inference disaggregation," arXiv preprint arXiv:2506.05508, 2025.

[82] MLCommons, "MLPerf inference v5.0 datacenter results (closed division)," https://github.com/mlcommons/inference_results_v5.0, Apr. 2025, published 2025-04-02. Accessed 2026-09-28.

[83] MLCommons, "MLPerf inference v5.1 datacenter results (closed division)," https://github.com/mlcommons/inference_results_v5.1, Sep. 2025, published 2025-09-09. Accessed 2026-09-28.

[84] MLCommons, "MLPerf inference v6.0 datacenter results (closed division)," https://github.com/mlcommons/inference_results_v6.0, Apr. 2026, published 2026-04-01. Accessed 2026-09-28.

[85] MLCommons, "MLPerf inference v6.1 datacenter results (closed division)," https://github.com/mlcommons/inference_results_v6.1, Sep. 2026, published 2026-09-16; includes preview systems. Accessed 2026-09-28.

[86] Moonshot AI, "Kimi K2.6," https://huggingface.co/moonshotai/Kimi-K2.6, 2026, model card and weights; accessed 2026-07-16.

[87] J. Morales, "Sohu AI chip claimed to run models 20x faster and cheaper than NVIDIA H100 GPUs," Tom's Hardware, https://www.tomshardware.com/tech-industry/artificial-intelligence/sohu-ai-chip-claimed-to-run-models-20x-faster-and-cheaper-than-nvidia-h100-gpus, Jun. 2024, coverage of Etched's Sohu transformer-ASIC announcement; the original vendor announcement page has since been removed. Accessed 2026-07-29.

[88] T. P. Morgan, "Taalas etches AI models onto transistors to rocket boost inference," The Next Platform, https://www.nextplatform.com/2026/02/19/taalas-etches-ai-models-onto-transistors-to-rocket-boost-inference/, Feb. 2026, HC1: a hardwired Llama-3.1-8B model-as-silicon ASIC. Accessed 2026-07-29.

[89] P. J. Nair, R. Hadidi, S. Ganesh, S. Kodge, S. Rathore, N. Thanawala, N. Reddy, G. Saharia, V. Patankar, A. Tiruvur, N. Kurella, and S. Bhoja, "Early silicon of Raptor: The first 3D-DRAM accelerator for generative inference," in *Proceedings of the 53rd Annual ACM/IEEE International Symposium on Computer Architecture (ISCA)*, Raleigh, NC, USA, 2026, pp. 2632–2647.

[90] D. Narayanan, M. Shoeybi, J. Casper, P. LeGresley, M. Patwary, V. Korthikanti, D. Vainbrand, P. Kashinkunti, J. Bernauer, B. Catanzaro, A. Phanishayee, and M. Zaharia, "Efficient large-scale language model training on GPU clusters using Megatron-LM," in *Proceedings of the International Conference for High Performance Computing, Networking, Storage and Analysis (SC)*, 2021.

[91] S. Nie, F. Zhu, Z. You, X. Zhang, J. Ou, J. Hu, J. Zhou, Y. Lin, J.-R. Wen, and C. Li, "Large language diffusion models," in *Advances in Neural Information Processing Systems 38 (NeurIPS)*, 2025, arXiv:2502.09992.

[92] T. Nowatzki, J. Menon, C.-H. Ho, and K. Sankaralingam, "Architectural simulators considered harmful," *IEEE Micro*, vol. 35, no. 6, pp. 4–12, 2015.

[93] NVIDIA, "NVIDIA A100 Tensor Core GPU," Data sheet, https://www.nvidia.com/content/dam/en-zz/Solutions/Data-Center/a100/pdf/nvidia-a100-datasheet-nvidia-us-2188504-web.pdf, May 2022, 80 GB SXM and PCIe specifications. Accessed 2026-07-30.

[94] NVIDIA, "NVIDIA GB200 NVL72," https://www.nvidia.com/en-us/data-center/gb200-nvl72/, 2024, product page, accessed 2026-07-14. 72 Blackwell GPUs + 36 Grace CPUs; 13.4 TB HBM3e; 576 TB/s aggregate memory bandwidth; NVLink 5 at 1.8 TB/s GPU-to-GPU and 130 TB/s rack; 120 kW rack (nominal).

[95] NVIDIA, "NVIDIA H200 Tensor Core GPU," https://www.nvidia.com/en-us/data-center/h200/, 2024, product page, accessed 2026-07-14. 141 GB HBM3e, 4.8 TB/s, 900 GB/s NVLink; SXM 3,958 TFLOPS FP8/INT8 WITH SPARSITY (dense FP8 = 1,979), 700 W.

[96] NVIDIA, "NVIDIA announces Spectrum-X photonics, co-packaged optics networking switches to scale AI factories to millions of GPUs," NVIDIA Newsroom, https://nvidianews.nvidia.com/news/nvidia-spectrum-x-co-packaged-optics-networking-switches-ai-factories, Mar. 2025, announced at GTC, 2025-03-18.

[97] NVIDIA, "NVIDIA Dynamo: A datacenter scale distributed inference serving framework," https://github.com/ai-dynamo/dynamo, 2025, software; no associated publication. Accessed 2026-07-16.

[98] NVIDIA, "NVIDIA GB300 NVL72," Product specification page, https://www.nvidia.com/en-us/data-center/gb300-nvl72/, 2025, Blackwell Ultra rack-scale platform. Accessed 2026-07-30.

[99] NVIDIA, "NVIDIA unveils NVLink Fusion for industry to build semi-custom AI infrastructure with NVIDIA partner ecosystem," NVIDIA Newsroom, https://nvidianews.nvidia.com/news/nvidia-nvlink-fusion-semi-custom-ai-infrastructure-partner-ecosystem, May 2025, published 2025-05-18; accessed 2026-09-28.

[100] NVIDIA, "NVIDIA unveils Rubin CPX: A new class of GPU designed for massive-context inference," NVIDIA Newsroom, https://nvidianews.nvidia.com/news/nvidia-unveils-rubin-cpx-a-new-class-of-gpu-designed-for-massive-context-inference, Sep. 2025, announced 2025-09-09. 128 GB GDDR7, 30 PFLOPS NVFP4; positioned to "disaggregate the context processing from the generation" with a Rubin GPU doing token generation, linked through a KV cache. Used here as a prospective-roadmap example, not as a claim about shipping status.

[101] NVIDIA, "TensorRT-LLM performance overview," https://github.com/NVIDIA/TensorRT-LLM/blob/1ffa2c893720ca2c3c6d245829b0c493485d21a6/docs/source/developer-guide/perf-overview.md, Dec. 2025, release 1.1 tables, commit 1ffa2c8 (2025-12-16), unchanged through 2026-09-11; accessed 2026-09-28.

[102] NVIDIA, "NVIDIA NVLink and NVLink switch," Product specification page, https://www.nvidia.com/en-us/data-center/nvlink/, 2026, accessed 2026-09-28. Fifth generation: 1,800 GB/s per GPU, 8- or 72-GPU domains, SHARP engines in each NVLink Switch; sixth generation: 3,000 GB/s per GPU, 216 TB/s per NVL72 (preliminary). Bidirectional per-GPU figures.

[103] NVIDIA, "NVIDIA scalable hierarchical aggregation and reduction protocol (SHARP)," NVIDIA Networking Documentation, https://networking-docs.nvidia.com/sharpum/3140, 2026, documents in-network collective offload and reduction; accessed 2026-07-31.

[104] NVIDIA, "NVIDIA Vera Rubin datasheet," https://dam-cdn.nvd.orangelogic.com/AssetLink/56p68o47y6f1yucpubl0ump1c0aif422.pdf,

2026, PDF dated 2026-06-22, snapshot accessed 2026-09-28. p. 7: benchmark power assumption 1800 W/GPU (Vera Rubin NVL4); p. 9: per-GPU table (22 TB/s, 3.6 TB/s). The live download was revised by 2026-10-09.

[105] NVIDIA, "NVIDIA Vera Rubin NVL72: Rack-scale agentic AI supercomputer," NVIDIA product specification page, https://www.nvidia.com/en-us/data-center/vera-rubin-nvl72/, 2026, accessed 2026-09-28. Per GPU: 288 GB HBM4 at 19.2 TB/s; 17.5 PFLOPS dense FP8/FP6; NVFP4 50 PFLOPS inference (sparse) and 35 training (dense); NVLink 3 TB/s. Revised between 2026-09-01 and 2026-09-11 from 22 TB/s and 3.6 TB/s; archived 2026-07-17 state: http://web.archive.org/web/20260717095244/https://www.nvidia.com/en-us/data-center/vera-rubin-nvl72/.

[106] NVIDIA, "NVIDIA Vera Rubin POD: Seven chips, five rack-scale systems, one AI supercomputer," NVIDIA Technical Blog, https://developer.nvidia.com/blog/nvidia-vera-rubin-pod-seven-chips-five-rack-scale-systems-one-ai-supercomputer/, 2026, describes the prospective Vera Rubin Ultra NVL576 system. Accessed 2026-07-30.

[107] NVIDIA TensorRT LLM Team, "How to get best performance on DeepSeek-R1 in TensorRT-LLM," https://github.com/NVIDIA/TensorRT-LLM/blob/8a9c66ce086594054d3722307cfed2d658d25e60/docs/source/blogs/Best_perf_practice_on_DeepSeek-R1_in_TensorRT-LLM.md, 2025, created 2025-04-10; read at commit 8a9c66c. Accessed 2026-09-28.

[108] NVIDIA TensorRT LLM Team, "Pushing latency boundaries: Optimizing DeepSeek-R1 performance on NVIDIA B200 GPUs," https://nvidia.github.io/TensorRT-LLM/blogs/tech_blog/blog1_Pushing_Latency_Boundaries_Optimizing_DeepSeek-R1_Performance_on_NVIDIA_B200_GPUs.html, May 2025, accessed 2026-09-28.

[109] NVIDIA TensorRT LLM Team, "Running a high performance GPT-OSS-120B inference server with TensorRT LLM," https://nvidia.github.io/TensorRT-LLM/blogs/tech_blog/blog9_Deploying_GPT_OSS_on_TRTLLM.html, Aug. 2025, accessed 2026-09-28.

[110] OpenAI, "gpt-oss-120b & gpt-oss-20b model card," arXiv preprint arXiv:2508.10925, 2025.

[111] J. Park, J. Choi, K. Kyung, M. J. Kim, Y. Kwon, N. S. Kim, and J. H. Ahn, "AttAcc! Unleashing the power of PIM for batched transformer-based generative model inference," in *Proceedings of the 29th ACM International Conference on Architectural Support for Programming Languages and Operating Systems (ASPLOS)*, 2024, pp. 103–119.

[112] P. Patel, E. Choukse, C. Zhang, Í. Goiri, B. Warrier, N. Mahalingam, and R. Bianchini, "Characterizing power management opportunities for LLMs in the cloud," in *Proceedings of the 29th ACM International Conference on Architectural Support for Programming Languages and Operating Systems (ASPLOS)*, 2024, pp. 207–222.

[113] P. Patel, E. Choukse, C. Zhang, A. Shah, Í. Goiri, S. Maleki, and R. Bianchini, "Splitwise: Efficient generative LLM inference using phase splitting," in *Proceedings of the 51st Annual International Symposium on Computer Architecture (ISCA)*, 2024, pp. 118–132.

[114] R. Pope, S. Douglas, A. Chowdhery, J. Devlin, J. Bradbury, A. Levskaya, J. Heek, K. Xiao, S. Agrawal, and J. Dean, "Efficiently scaling transformer inference," in *Proceedings of Machine Learning and Systems (MLSys)*, 2023.

[115] Positron, "Asimov inference accelerator," Product page, https://www.positron.ai/asimov, 2026, memory capacity, realizable memory bandwidth and power; announced for 2027. Accessed 2026-09-29.

[116] R. Prabhakar, R. Sivaramakrishnan, D. Gandhi, Y. Du, M. Wang, X. Song, K. Zhang, T. Gao, A. Wang, X. Li, Y. Sheng, J. Brot, D. Sokolov, A. Vivek, C. Leung, A. Sabnis, J. Bai, T. Zhao, M. Gottscho, D. Jackson, M. Luttrell, M. K. Shah, Z. Chen, K. Liang, S. Jain, U. Thakker, D. Huang, S. Jairath, K. J. Brown, and K. Olukotun, "SambaNova SN40L: Scaling the AI memory wall with dataflow and composition of experts," in *Proceedings of the 57th IEEE/ACM International Symposium on Microarchitecture (MICRO)*, 2024, pp. 1353–1366.

[117] R. Qin, Z. Li, W. He, J. Cui, F. Ren, M. Zhang, Y. Wu, W. Zheng, and X. Xu, "Mooncake: Trading more storage for less computation — a KVCache-centric architecture for serving LLM chatbot," in *Proceedings of the 23rd USENIX Conference on File and Storage Technologies (FAST)*, 2025, pp. 155–170.

[118] C. Qiu, X. Fu, F. Li, Y. Qian, Y. Xie, X. Cai, Y. Shan, Y. Wu, and M. Zhang, "AFD-Ledger: Deployment provisioning for attention–FFN disaggregation," arXiv preprint arXiv:2608.04502, 2026, version 1, 2026-08-05.

[119] Z. Qiu, Z. Wang, B. Zheng, Z. Huang, K. Wen, S. Yang, R. Men, L. Yu, F. Huang, S. Huang, D. Liu, J. Zhou, and J. Lin, "Gated attention for large language models: Non-linearity, sparsity, and attention-sink-free," in *Advances in Neural Information Processing Systems 38 (NeurIPS)*, 2025, arXiv:2505.06708.

[120] Qwen Team, "Qwen3 technical report," arXiv preprint arXiv:2505.09388, 2025.

[121] Qwen Team, "Qwen3.5-397B-A17B," https://huggingface.co/Qwen/Qwen3.5-397B-A17B, 2026, model card and weights; accessed 2026-07-16.

[122] K. Ray, N. M. Gonzalez, B. Wassermann, R. Tzoref-Brill, and D. H. Lorenz, "Statistical modeling and uncertainty estimation of LLM inference systems," arXiv preprint arXiv:2505.09319, 2025.

[123] Rebellions, "ATOM: 5nm versatile inference SoC," Product brief, https://rebellions.ai/wp-content/uploads/2023/02/Rebellions_ATOM_Product-Brief_2023.pdf, 2023, accelerator architecture and specifications. Accessed 2026-07-30.

[124] Rebellions, "REBEL (RBLN-CR13)," Product brief, https://rebellions.ai/wp-content/uploads/2024/11/Rebellions_REBEL_Product-brief_2024.pdf, 2024, HBM3e chiplet accelerator specifications. Accessed 2026-07-30.

[125] SemiAnalysis, "InferenceX: Open source continuous inference benchmark," https://inferencex.semianalysis.com/, 2026, formerly InferenceMAX; Apache-2.0, code at https://github.com/SemiAnalysisAI/InferenceX. Frozen export of 2026-09-28 (public API; weekly database release `db-dump/2026-09-28`). B200 calibration anchor: run of 2025-10-29 (`llama70b`, FP8, 1K/1K, TensorRT-LLM, 8 GPUs at TP8, concurrency 4), export of July 2026.

[126] SGLang Project, "PD disaggregation," SGLang Documentation, https://docs.sglang.io/docs/advanced_features/pd_disaggregation, 2026, documentation; accessed 2026-10-08.

[127] Y. S. Shao, B. Reagen, G.-Y. Wei, and D. M. Brooks, "Aladdin: A pre-RTL, power-performance accelerator simulator enabling large design space exploration of customized architectures," in *Proceedings of the 41st Annual International Symposium on Computer Architecture (ISCA)*, 2014, pp. 97–108.

[128] N. Shazeer, "Fast transformer decoding: One write-head is all you need," arXiv preprint arXiv:1911.02150, 2019.

[129] N. Shazeer, A. Mirhoseini, K. Maziarz, A. Davis, Q. Le, G. Hinton, and J. Dean, "Outrageously large neural networks: The sparsely-gated mixture-of-experts layer," in *Proceedings of the 5th International Conference on Learning Representations (ICLR)*, 2017.

[130] S. Shen, A. Korzh, J. Bachan, T. Chen, A. Goel, L. Schneider, P. Kousha, Z. He, S. Jeaugey, K. Iskra, N. Chandawala, J. R. Hammond, and T. Hoefler, "Every microsecond matters: Achieving near speed-of-light latency in GPU collectives," arXiv preprint arXiv:2607.16100, 2026.

[131] C. Song, M. Wang, H. Zhou, H. Liang, Y. Lyu, Z. Chen, Y. Fan, and Z. Zhou, "Analytical provisioning for attention-FFN disaggregated LLM serving under stochastic workloads," arXiv preprint arXiv:2601.21351, 2026, version 4, revised 2026-08-14.

[132] StepFun Team, "Step-3 is large yet affordable: Model-system co-design for cost-effective decoding," arXiv preprint arXiv:2507.19427, 2025.

[133] Synopsys, "Platform architect: SoC architecture analysis and optimization," Product documentation, https://www.synopsys.com/verification/virtual-prototyping/platform-architect.html, 2026, accessed 2026-10-08.

[134] Tenstorrent, "Blackhole PCIe cards," Tenstorrent hardware documentation, https://docs.tenstorrent.com/aibs/blackhole/index.html, 2026, Blackhole p150 family specifications. Accessed 2026-07-30.

[135] Tenstorrent, "Wormhole PCIe cards," Tenstorrent hardware documentation, https://docs.tenstorrent.com/aibs/wormhole/index.html, 2026, Wormhole n300 family specifications. Accessed 2026-07-30; link checked 2026-10-09.

[136] The Mooncake Team, "Deploying Kimi K2 with PD disaggregation and large-scale expert parallelism on 128 H200 GPUs," LMSYS Org Blog, https://www.lmsys.org/blog/2025-07-20-k2-large-scale-ep/, Jul. 2025, accessed 2026-09-28.

[137] The SGLang Team, "Deploying DeepSeek on GB200 NVL72 with PD and large scale EP (Part II): 3.8x prefill, 4.8x decode throughput," LMSYS Org Blog, https://www.lmsys.org/blog/2025-09-25-gb200-part-2/, Sep. 2025, accessed 2026-09-28.

[138] The SGLang Team, "Deploying DeepSeek with PD disaggregation and large-scale expert parallelism on 96 H100 GPUs," LMSYS Org Blog, https://www.lmsys.org/blog/2025-05-05-large-scale-ep/, May 2025, published 2025-05-05; accessed 2026-09-28.

[139] A. Tirumala and R. Wong, "NVIDIA Blackwell platform: Advancing generative AI and accelerated computing," in *2024 IEEE Hot Chips 36 Symposium (HCS)*, 2024, pp. 1–33.

[140] A. Tschand, Y. Fu, V. S. Mailthody, N. Oswald, P.-A. Tsai, R. Zhao, O. Villa, V. J. Reddi, and K. Sankaralingam, "Rethinking heterogeneous system disaggregation for subquadratic attention," arXiv preprint arXiv:2609.13134, 2026, version 1, 2026-09-11.

[141] Untether AI, "speedAI240 accelerator," Product page, https://www.untether.ai/products/, 2024, at-memory accelerator and card specifications. Accessed 2026-07-30; archived 2026-01-14 state: http://web.archive.org/web/20260114211406/https://www.untether.ai/products/.

[142] S. Usami, V. Vishwanath, and E. W. Bethel, "Prefill/decode-aware evaluation of LLM inference on emerging AI accelerators," in *Workshop on HPC for AI Foundation Models & LLMs for Science (HPAI4S), co-located with IEEE IPDPS*, 2026, arXiv:2606.17104.

[143] vLLM Project, "Disaggregated prefilling (experimental)," vLLM Documentation, https://docs.vllm.ai/en/stable/features/disagg_prefill/, 2026, documentation; accessed 2026-10-08.

[144] vLLM Project, "Engine arguments: `--gpu-memory-utilization`," https://docs.vllm.ai/en/stable/configuration/engine_args/, 2026, default 0.9 in `vllm/config/cache.py` through v0.19.0 (2026-04-03); 0.92 from v0.20.0 (2026-04-27) to v0.30.0 (2026-09-22). Accessed 2026-09-28.

[145] C. Wang, P. Zuo, Z. Chen, Y. Liang, Z. Yu, and M.-C. Yang, "Prefill-decode aggregation or disaggregation? Unifying both for goodput-optimized LLM serving," arXiv:2508.01989, 2025.

[146] Z. Wang, Z. Wang, F. Fu, Y. Lu, J. Hou, Y. Chen, X. Shen, H. Liu, X. Li, J. Chen, R. Gu, D. Wang, Z. Tan, Y. Cheng, H. Zhang, X. Huang, P. Zhang, and X. Hu, "Demystifying the design space and best practices for heterogeneous LLM inference and serving," arXiv preprint arXiv:2606.29708, 2026, version 2, revised 2026-06-30.

[147] Z. Wei, Y. Wang, J. Yen, M. Xia, and Z. Qi, "HBM is not all you need: Efficient disaggregated LLM serving across memory-heterogeneous accelerators," arXiv preprint arXiv:2606.29986, 2026.

[148] S. Weidman, K. Devleker, and A. Ling, "How NVIDIA Groq 3 LPX unlocks ultrafast interactivity at long context on NVIDIA Vera Rubin," NVIDIA Technical Blog, https://developer.nvidia.com/blog/how-nvidia-groq-3-lpx-unlocks-ultrafast-interactivity-at-long-context-on-nvidia-vera-rubin/, Aug. 2026, published 2026-08-24; accessed 2026-09-28.

[149] S. Williams, A. Waterman, and D. A. Patterson, "Roofline: An insightful visual performance model for multicore architectures," *Communications of the ACM*, vol. 52, no. 4, pp. 65–76, 2009.

[150] H. Wu, A. R. Bambhaniya, S. Banerjee, T. Khare, S. Srinivasan, S. Subramanian, S. Kundu, M. Kumar, M. Elavazhagan, W. Won, A. Yazdanbakhsh, and T. Krishna, "How far can disaggregation go? A design-space exploration of attention-FFN disaggregation for efficient MoE LLM serving," arXiv preprint arXiv:2605.28302, 2026.

[151] R. E. Wunderlich, T. F. Wenisch, B. Falsafi, and J. C. Hoe, "SMARTS: Accelerating microarchitecture simulation via rigorous statistical sampling," in *Proceedings of the 30th Annual International Symposium on Computer Architecture (ISCA)*, 2003, pp. 84–95.

[152] xDeepServe (XDS) Team @ Huawei, "Huawei cloud model-as-a-service on the CloudMatrix384 SuperPod," arXiv preprint arXiv:2508.02520, 2025, version 6, revised 2026-03-01.

[153] T. Xu, Y. Liu, X. Lu, Y. Zhao, X. Zhou, A. Feng, Y. Chen, Y. Shen, Q. Zhou, X. Chen, I. Sherstyuk, H. Li, R. Thakkar, B. Hamm, Y. Li, X. Huang, W. Wu, A. Shanbhag, H. Kim, C. Chen, and J. Lai, "AIConfigurator: Lightning-fast configuration optimization for multi-framework LLM serving," arXiv preprint arXiv:2601.06288, 2026, version 1, 2026-01-09.

[154] J. J. Yi, D. J. Lilja, and D. M. Hawkins, "A statistically rigorous approach for improving simulation methodology," in *Proceedings of the 9th International Symposium on High-Performance Computer Architecture (HPCA)*, 2003, pp. 281–291.

[155] L. Yin and K. Bao, "SGLang for gpt-oss: From day 0 support to enhanced performance," LMSYS Org Blog, https://lmsys.org/blog/2025-08-27-gpt-oss/, Aug. 2025, accessed 2026-09-28.

[156] Z. Yu, H. Ye, C. Zhou, O. R. Venkatachalam, Z. Pan, Z. Hu, J. Kim, W. W. Ro, P.-A. Tsai, S. Pei, Y. Kang, and Y. Ding, "AMMA: A multi-chiplet memory-centric architecture for low-latency 1M context attention serving," in *Proceedings of the 59th IEEE/ACM International Symposium on Microarchitecture (MICRO)*, 2026, to appear; arXiv:2604.26103.

[157] J. Yuan, H. Gao, D. Dai, J. Luo, L. Zhao, Z. Zhang, Z. Xie, Y. Wei, L. Wang, Z. Xiao, Y. Wang, C. Ruan, M. Zhang, W. Liang, and W. Zeng, "Native sparse attention: Hardware-aligned and natively trainable sparse attention," in *Proceedings of the 63rd Annual Meeting of the Association for Computational Linguistics (ACL), Volume 1: Long Papers*, 2025, pp. 23 078–23 097.

[158] H. Zhang, A. Ning, R. B. Prabhakar, and D. Wentzlaff, "LLMCompass: Enabling efficient hardware design for large language model inference," in *Proceedings of the 51st Annual International Symposium on Computer Architecture (ISCA)*, 2024, pp. 1080–1096.

[159] H. Zhang, P. Patel, A. Ning, and D. Wentzlaff, "SPAD: Specialized prefill and decode hardware for disaggregated LLM inference," arXiv preprint arXiv:2510.08544, 2025.

[160] Z. Zhang, Y. Wang, Y. Zhao, J. Xiao, Q. Yang, X. Wang, J. Jiang, Q. Weng, R. Chen, S. Shi, Y. Chen, and M. Yu, "Janus: Disaggregating attention and experts for scalable MoE inference," arXiv preprint arXiv:2512.13525, 2025, version 4, revised 2026-08-11.

[161] Y. Zhong, S. Liu, J. Chen, J. Hu, Y. Zhu, X. Liu, X. Jin, and H. Zhang, "DistServe: Disaggregating prefill and decoding for goodput-optimized large language model serving," in *Proceedings of the 18th USENIX Symposium on Operating Systems Design and Implementation (OSDI)*, 2024, pp. 193–210.

[162] R. Zhu, Z. Jiang, C. Jin, P. Wu, C. A. Stuardo, D. Wang, X. Zhang, H. Zhou, H. Wei, Y. Cheng, J. Xiao, X. Zhang, L. Liu, H. Lin, L.-W. Chang, J. Ye, X. Yu, X. Liu, X. Jin, and X. Liu, "MegaScale-Infer: Efficient mixture-of-experts model serving with disaggregated expert parallelism," in *Proceedings of the ACM SIGCOMM 2025 Conference*, 2025, pp. 592–608.

[163] P. Zuo, H. Lin, J. Deng, N. Zou, X. Yang, Y. Diao, W. Gao, K. Xu, Z. Chen, S. Lu, Z. Qiu, P. Li, X. Chang, Z. Yu, F. Miao, J. Zheng, Y. Li, Y. Feng, B. Wang, Z. Zong, M. Zhou, W. Zhou, H. Chen, X. Liao, Y. Li, W. Zhang, P. Zhu, Y. Wang, C. Xiao, D. Liang, D. Cao, J. Liu, Y. Yang, X. Bai, Y. Li, H. Xie, H. Wu, Z. Yu, L. Chen, H. Liu, Y. Ding, H. Zhu, J. Xia, Y. Xiong, Z. Yu, and H. Liao, "Serving large language models on Huawei CloudMatrix384," arXiv preprint arXiv:2506.12708, 2025, version 1, 2025-06-15.

AI USE

AI systems assisted with manuscript preparation and code development. All AI-assisted text, code, and results were independently reviewed, revised, and verified by the authors, who take full responsibility for this paper.